Contents

Section 1. General Information 4

Materials 4

Instruments and measurements 8

Preparation of duplexes L_iL_i', L_fL_f', A_1A_1', B_1B_1', B_1B_2', C_1C_1', and C_1C_2' 8

Preparation of templates T_1, T_2, T_3, T_4, T_5, and T_6 8

Preparation of duplexes F_1Q_1, F_2Q_2, F_3Q_3, and F_4Q_4 8

Preparation of riboswitches rS_1, rS_2, and rS_3 8

Probing the conversion of L_i concentrations into discrete transcriptional states mediated by threshold-gated incoherent feedforward networks (TIFFNs) 9

Probing the decoding of light duration into discrete transcriptional states dictated by photochemical-integration programmable duration-decoding systems (piPDDSs) 9

Probing the persistence-selective of RNA inputs into discrete transcriptional states governed by a dissipative-filtering programmable duration-decoding system (dfPDDS) 10

Probing the decoding of light duration into discrete protein-output states dictated by the integrated piPDDS/riboswitch architectures 11

Probing L_i-concentration-dependent RNA-output-state selections in synthetic cells 12

Fluorescence data processing 12

Section 2. Design Principles of The Programmable Duration-Decoding Framework 14

Design of piPDDS-I 14

Design of piPDDS-II 14

Design of piPDDS-III 15

Design of dfPDDS-I 16

Design of the integrated piPDDS/riboswitch architectures. 17

Section 3. L_i-Concentration-Dependent RNA-Output-State Selections in Synthetic Cells 18

Programming L_i concentration-dependent RNA-output-states 18

L_i concentration-dependent RNA-output-state selections in synthetic cells 19

Section 4. Characterisations of PDDS-Dictated Decoding of Stimulus Duration into Discrete Transcriptional States 21

Calibration curve of L_i 21

Calibration curves of the released L_i under UV irradiation 22

TIFFN-I-dictated decoding of L_i concentration into discrete transcriptional states 23

TIFFN-II-dictated decoding of L_i concentration into discrete transcriptional states 24

TIFFN-III-dictated decoding of L_i concentration into discrete transcriptional states 25

TIFFN-I-mediated decoding of L_i concentration into discrete transcriptional states in the presence of additional 0.040 μM A_1' 26

TIFFN-I-governed decoding of L_i concentration into discrete transcriptional states in the presence of additional 0.040 μM A_1A_1' 27

TIFFN-II-mediated decoding of L_i concentration into discrete transcriptional states in the presence of additional 0.040 μM B_2' 28

TIFFN-II-governed decoding of L_i concentration into discrete transcriptional states in the presence of additional 0.040 μM B_1B_2' 29

piPDDS-I-dictated decoding of light duration into discrete transcriptional states 30

piPDDS-II-governed decoding of light duration into discrete transcriptional states 31

piPDDS-III-mediated decoding of light duration into discrete transcriptional states 32

Small reservoir-dictated dissipative RNA filtering transmits persistent RNA inputs into rP_5-output state 33

Large reservoir-dictated dissipative RNA filtering transmitting persistent RNA inputs into rP_6-output state 34

Reservoir-programmed L_f pulse dynamics 35

Calibration curve of L_f 35

Section 5. Characterisations of Duration-Decoding Programmed Distinct RNA-Output States in Synthetic Cells 36

Light-duration-dependent release of L_i in synthetic cells 36

TIFFN-I-mediated concentration-dependent differential transcription in synthetic cells 36

TIFFN-II-dictated concentration-dependent differential transcription in synthetic cells 37

TIFFN-III-dictated concentration-dependent differential transcription in synthetic cells 38

piPDDS-I-governed duration-dependent differential transcription in synthetic cells 38

piPDDS-I-governed duration-dependent differential transcription in synthetic cells in the presence of additional 0.16 μM A_1' 39

piPDDS-I-governed duration-dependent differential transcription in synthetic cells in the presence of additional 0.16 μM A_1A_1' 39

piPDDS-II-governed duration-dependent differential transcription in synthetic cells 40

piPDDS-III-governed duration-dependent differential transcription in synthetic cells 40

Section 6. Characterisations of Duration Decoding Driven Differential Protein Synthesis in Synthetic Cells 41

Duration-windowed activation of GFP expression dictated by the integrated piPDDS-I/GFP-regulating riboswitch architecture 41

Duration-windowed repression of GFP expression governed by the integrated piPDDS-II/GFP-regulating riboswitch architecture 42

Duration-decoding into distinct protein outputs mediated by the integrated piPDDS-III/GFP- and mCherry-regulating riboswitch architecture 43

piPDDS-III-governed duration-dependent differential protein synthesis in synthetic cells..... 44

Section 7. Characterisations of Duration-Windowed Lipid Membrane Permeabilisation 45

Baseline permeability of GUV lipid membranes in the absence of α-HL 45

piPDDS-I-governed duration-windowed membrane permeabilisation in synthetic cells 45

1. General Information

Materials. 1-palmitoyl-2-oleoyl-glycero-3-phosphocholine (POPC) was purchased from Avanti Polar Lipids (Alabaster, AL). Mineral oil was purchased from Sigma-Aldrich. Chloroform ($CHCl_3$) was purchased from Energy Chemical. T7 high-yield RNA synthesis kit was purchased from Yeasen Biotechnology (Shanghai) Co., Ltd. VAHTS RNA Clean Beads were obtained from Vazyme Biotech Co., Ltd. (Nanjing, China; Cat. No. N412). RNase H (5,000 $U \cdot mL^{-1}$), murine RNase inhibitor, rCutSmart® buffer (1× buffer components: 50 mM potassium acetate, 20 mM tris-acetate, 10 mM magnesium acetate, 100 $\mu g \cdot mL^{-1}$ recombinant albumin, pH 7.9 at 25 °C) and PURExpress *in vitro* protein synthesis kit (E6800, NEB) were purchased from New England BioLabs Inc. Malachite green (MG), TO1-3PEG-Biotin (TO-1) and cholesterol were purchased from Sigma-Aldrich. Cyanine 5 (Cy5) was purchased from MedChemExpress (MCE). Plasmid extraction was performed using the NucleoSpin Plasmid kit (Macherey-Nagel, 740588) following the manufacturer's instructions. A handheld UV lamp (LUYOR-3410, LUYOR) was used as the light source for photocleavage experiments. Ultrapure water (electric resistance, 18.2 MΩ·cm) obtained through a Millipore Milli-Q water purification system (Billerica, MA, USA) was used throughout the experiments. All DNA and RNA oligonucleotides were synthesized and high-performance liquid chromatography (HPLC) purified by Sangon Biotech Co. Ltd. (Shanghai, China).

The oligonucleic acid sequences used in the study are as follows:

L_i	L_{i-1}[a]	5′-GTGTTGTAAGTGGAAATGTGTGTCTTCTACTCTAGCCTCTGTGTGTGACTTTTGTTGTGAGTTTGAA-3′
	L_{i-2}[b]	5′-GTGTTGTATGTGGAAATGTGTGTCGACTTCTACTCTAGCCTCTGTGTGTGACCTTATGTTGTGAGTTTGAA-3′
L_i'	L_{i-1}'[c]	5′-ATTCAAACTC/iPC/ACAACAAAA/iPC/GTCACACAAGACACAC/iPC/ATTTCCACT/iPC/TACAACACA-3′
	L_{i-2}'[d]	5′-TTCAAACTC/iPC/ACAACATAA/iPC/GGTCACCGACACAC/iPC/ATTTCCACA/iPC/TACAACAC-3′
A_1		5′-ATGTGTGTTACTCTTGTGTGTGACTTTCTTCT-3′
B_1		5′-TGTGTGTCTTCTACTCTTGTGTGTGACCTTATGTTA-3′
C_1		5′-ATGTGTGTCGACTTCTACTCTTGTGTGTGACTTATGAGTT-3′
D		5′-TATTATTGATCACACAAGAGTAGAAGTCGACATCAAT-3′
A_1'		5′-TTCAAACTCACAACAAAGAAAGTCACACACAGAGGCTAGAGTAACACACATTTCCACTTACAACAC-3′
B_1'		5′-ACATAAGGTCACACACAGAGGCTAGAGTAGAAGACACACATTTCCACTT-3′

C_1'		5′-ACTCATAAGTCACACACAGAGGCTAGAGTAGAAGTCGACACAC ATTTCCACTTAC-3′
B_2'		5′-TTCAATGGAACAACTACATAAGGTCACACACAGAGGCTAGAGT AGAAGACACACATAACCAGATACATCAC-3′
C_2'		5′-ACTCATAAGTCACACACAGAGGCTAGAGTAGAAGTCGACACAC ATAACCAGTT-3′
T_1	T_{1-1}	5′-AGAAGAAAGTCAATCAATAATACGACTCACTATAGGGACCGTGG ACCGCATGAGGTCCACGGTAAACATAACTATAACAAGCCTACAATT CATTCAAAC-3′
	T_{1-2}	5′-GTTTGAATGAATTGTAGGCTTGTTATAGTTATGTTTACCGTGGAC CTCATGCGGTCCACGGTCCCTATAGTGAGTCG-3′
T_2	T_{2-1}	5′-TGTTAATTCAACATAAGGTCAATCAATAATACGACTCACTATAGG GTGATGGGACATTCCGATGTCCCATCAATAAGAGCAAGACAATGG TAAGTAGTAATAGATAAG-3′
	T_{2-2}	5′-CTTATCTATTACTACTTACCATTGTCTTGCTCTTATTGATGGGACAT CGGAATGTCCCATCACCCTATAGTGAGTCG-3′
T_3	T_{3-1}	5′-GAGTAAGTAAACTCATAAGTCAATCAATAATACGACTCACTATAG GGACCGTGGACCGCATGAGGTCCACGGTAAACATAACTATAACAA GCCTACAATTCATTCAAAC-3′
	T_{3-2}	5′-GTTTGAATGAATTGTAGGCTTGTTATAGTTATGTTTACCGTGGAC CTCATGCGGTCCACGGTCCCTATAGTGAGTCG-3′
T_4	T_{4-1}	5′-GAGTAAGTAAACTCATAAGTCAATCAATAATACGACTCACTATAG GGCCACGCGTTGTCCTATCAACGCGTGGAAATCGTATCATCATTCTA GTCAATCAAATTCAAAG-3′
	T_{4-2}	5′-CTTTGAATTTGATTGACTAGAATGATGATACGATTTCCACGCGTT GATAGGACAACGCGTGGCCCTATAGTGAGTCG-3′
F_1		5′-FAM-TCTACTCTAGCCTCTGTGTG-3′
Q_1		5′-AACAAAAGTCACACACAGAGGCTAGAGTAGA-BHQ1-3′
F_2		5′-FAM-ACATAACTATAACAAGCCTACAATTC-3′
Q_2		5′-GTTTGAATGAATTGTAGGCTTGTTATAGTTATGT-BHQ1-3′
F_3		5′-ROX-AGCAAGACAATGGTAAGTAGTA-3′
Q_3		5′-CTTATCTATTACTACTTACCATTGTCTTGCT-BHQ2-3′
F_4		5′-Cy5-GTATCATCATTCTAGTCAATCAA-3′
Q_4		5′-CTTTGAATTTGATTGACTAGAATGATGATAC-BHQ2-3′
rI		5′-AAGAAAACAAGCAAAGUGUUGUAAAAUGUGUGUUCUAUGCU UUUGUUAGUUUGAACCGAAACCGUAAAAAUCCUCCGC-3′

L_f		5′-AAGAAAACAAGCAAAGTGTTGTAAGTGGAAATGTGTGTCTTCT ACTCTAGCCTCTGTGTGTGACTTTTGTTGTGAGTTTGAACCGAAAC CGTA-3′
L_f'		5′-GCGGAGGATTTTTACGGTTTCGGTTCAAACTAACAAAAGCACA CAGAGAGAGTAGAACACACATTTTACAACACTTTGCTTGTTTTCT TGCT-3′
T_5	T_{5-1}	5′-AGAAGAAAGTCAATCAATAATACGACTCACTATAGGATCCCGAC TGGCGAGAGCCAGGTAACGAATGGATCC-3′
	T_{5-2}	5′-GGATCCATTCGTTACCTGGCTCTCGCCAGTCGGGATCCTATAGTG AGTCG-3′
T_6	T_{6-1}	5′-TGTTAATTCAACATAAGGTCAATCAATAATACGACTCACTATAGG GCGTACGAAGGAGAGGAGAGGAAGAGGAGAGTACGC-3′
	T_{6-2}	5′-GCGTACTCTCCTCTTCCTCTCCTCTCCTTCGTACGCCCTATAGTGA GTCG-3′
Chol-DNA		5′-FAM-ATGATCATCACAA-Chol-3′
rS_1		5′-GUGAAUGAAUUGUAGGCUUGUUAUAGUUAUGAACAGAGGAG ACAUAACAUGAACAAGCCUAACCUGGCGGCAGCGCAAAAGAUG GUGAGUAAAGGUGAAGAACUGUUCACCGGUGUUGUUCCGAUCC UGGUUGAACUGGAUGGUGAUGUUAACGGCCACAAAUUCUCUGU UCGUGGUGAAGGUGAAGGUGAUGCAACCAACGGUAAACUGACC CUGAAAUUCAUCUGCACUACCGGUAAACUGCCGGUUCCAUGGCC GACUCUGGUGACUACCCUGACCUAUGGUGUUCAGUGUUUUUCU CGUUACCCGGAUCACAUGAAGCAGCAUGAUUUCUUCAAAUCUG CAAUGCCGGAAGGUUAUGUACAGGAGCGCACCAUUUCUUUCAA AGACGAUGGCACCUACAAAACCCGUGCAGAGGUUAAAUUUGAA GGUGAUACUCUGGUGAACCGUAUUGAACUGAAAGGCAUUGAUU UCAAAGAGGACGGCAACAUCCUGGGCCACAAACUGGAAUAUAA CUUCAACUCCCAUAACGUUUACAUCACCGCAGACAAACAGAAGA ACGGUAUCAAAGCUAACUUCAAAAUUCGCCAUAACGUUGAAGA CGGUAGCGUACAGCUGGCGGACCACUACCAGCAGAACACUCCGA UCGGUGAUGGUCCGGUUCUGCUGCCGGAUAACCACUACCUGUCC ACCCAGUCUAAACUGUCCAAAGACCCGAACGAAAAGCGCGACCA CAUGGUGCUGCUGGAGUUCGUUACUGCAGCAGGUAUCACGCAC GGCAUGGAUGAACUCUACAAAUAAUAAAACAGUCGAGCCCAGC GUGGUUAAACACU-3′

rS_2	5′-GAUCUAUUACUACUUACCAUUGUCUUGCUCUAUACAGAAACAGAGGAGAUAUAGAAUGAGACAAUGGAACCUGGCGGCAGCGCAAAAGAUGCGUAAAAUGGUGAGCAAGGGCGAGGAGGAUAACAUGGCCAUCAUCAAGGAGUUCAUGCGCUUCAAGGUUCACAUGGAGGGCUCCGUGAACGGCCACGAGUUCGAGAUCGAGGGCGAGGGCGAGGGCCGCCCCUACGAGGGCACCCAGACCGCCAAGCUGAAGGUGACCAAGGGUGGCCCCCUGCCCUUCGCCUGGGACAUCCUGUCCCCUCAGUUCAUGUACGGCUCCAAGGCCUACGUGAAGCACCCCGCCGACAUCCCCGACUACUUGAAGCUGUCCUUCCCCGAGGGCUUCAAGUGGGAGCGCGUGAUGAACUUCGAGGACGGCGGCGUGGUGACCGUGACCCAGGACUCCUCCCUGCAAGACGGCGAGUUCAUCUACAAGGUGAAGCUGCGCGGCACCAACUUCCCCUCCGACGGCCCCGUAAUGCAGAAGAAGACUAUGGGCUGGGAGGCCUCCUCCGAGCGGAUGUACCCCGAGGACGGCGCGCUGAAGGGCGAGAUCAAGCAGAGGCUGAAGCUGAAGGACGGCGGCCACUACGACGCUGAGGUCAAGACCACCUACAAGGCCAAGAAGCCCGUGCAACUGCCCGGCGCGUACAACGUCAACAUCAAGUUGGACAUCACCUCCCACAACGAGGACUACACCAUCGUGGAACAGUACGAACGCGCCGAGGGCCGCCACUCCACCGGCGGCAUGGACGAGCUGUACAAGUAAUAAAACAGUCGAGCCCAGCGUGGUUAAACACU-3′
rS_3	5′-GUGAAUGAAUUGUAGGCUUGUUAUAGUUAUGAACAGAGGAGACAUAACAUGAACAAGCCUAACCUGGCGGCAGCGCAAAAGAUGGCAGAUUCUGAUAUUAAUAUUAAAACCGGUACUACAGAUAUUGGAAGCAAUACUACAGUAAAAACAGGUGAUUUAGUCACUUAUGAUAAAGAAAAUGGCAUGCACAAAAAAGUAUUUUAUAGUUUUAUCGAUGAUAAAAAUCACAAUAAAAAACUGCUAGUUAUUAGAACAAAAGGUACCAUUGCUGGUCAAUAUAGAGUUUAUAGCGAAGAAGGUGCUAACAAAAGUGGUUUAGCCUGGCCUUCAGCCUUUAAGGUACAGUUGCAACUACCUGAUAAUGAAGUAGCUCAAAUAUCUGAUUACUAUCCAAGAAAUUCGAUUGAUACAAAAGAGUAUAUGAGUACUUUAACUUAUGGAUUCAACGGUAAUGUUACUGGUGAUGAUACAGGAAAAAUUGGCGGCCUUAUUGGUGCAAAUGUUUCGAUUGGUCAUACACUGAAAUAUGUUCAACCUGAUUUCAAAACAAUUUUAGAGAGCCCAACUGAUAAAAAAGUAGGCUGGAAAGUGAUAUUUAACAAUAUGGUGAAUCAAAAUUGGGGACCAUACGAUCGAGAUUCUUGGAACCCGGUAUAUGGCAAUCAACUUUUCAUGAAAACUAGAAAUGGUUCUAUGAAAGCAGCAGAUAACUUCCUUGAUCCUAACAAAGCAAGUUCUCUAUUAUCUUCAGGGUUUUCACCAGACUUCGCUACAGUUAUUACUAUGGAUAGAAAAGCAUCCAAACAACAAACAAA

	UAUAGAUGUAAUAUACGAACGAGUUCGUGAUGAUUACCAAUUG CAUUGGACUUCAACAAAUUGGAAAGGUACCAAUACUAAAGAUA AAUGGACAGAUCGUUCUUCAGAAAGAUAUAAAAUCGAUUGGGA AAAAGAAGAAAUGACAAAUUAAAACAGUCGAGCCCAGCGUGGU UAAACACU-3′

iPC denotes an internal photocleavable linker. The RBS sequence is underlined. [a]L_{i-1} was used in TIFFN-I/III and piPDDS-I/III. [b]L_{i-2} was used in TIFFN-II and piPDDS-II. [c]L_{i-1}′ was used in piPDDS-I/III. [d]L_{i-2}′ was used in piPDDS-II.

Instruments and measurements.

Fluorescence experiments. Fluorescence kinetics were measured at 37 °C on a Cary Eclipse Fluorometer (Varian Inc.). Excitations of FAM, ROX, and Cy5 were performed at 496, 588, and 648 nm, and emissions were recorded at 516, 608, and 668 nm, respectively. Excitations of TO-1 and MG were performed at 510 and 620 nm, and emissions were recorded at 535 and 650 nm, respectively.

Fluorescence microscopy experiments. Samples were homogenized by pipetting and transferred onto optical imaging dishes (NEST Biotechnology) prior to imaging. Fluorescence images were acquired using a Zeiss Axio Scope A1 microscope equipped with 488 nm, 543 nm, and 633 nm excitation light sources. Image analysis was performed using ImageJ software.

Preparation of duplexes L_iL_i', L_fL_f', A_1A_1', B_1B_1', B_1B_2', C_1C_1', and C_1C_2'. Taking L_iL_i' as an example, a mixture of L_i and L_i', 4.00 μM each, in 1× rCutSmart buffer, was annealed at 95 °C for 5 min, cooled down to 25 °C at a rate of 0.58 °C·min^{-1}, and then allowed to equilibrate at 25 °C for 2 h to yield duplex L_iL_i'.

Preparation of templates T_1, T_2, T_3, T_4, T_5, and T_6. Taking template T_1 as an example, a mixture of $T_{1\text{-}1}$ and $T_{1\text{-}2}$, 4.00 μM each, in 1× rCutSmart buffer, was annealed at 95 °C for 5 min, cooled down to 25 °C at a rate of 0.58 °C·min^{-1}, and then allowed to equilibrate at 25 °C for 2 h to yield template T_1.

Preparation of duplexes F_1Q_1, F_2Q_2, F_3Q_3, and F_4Q_4. Taking F_1Q_1 as an example, a mixture of F_1 and Q_1, 10.00 μM each, in 1× rCutSmart buffer, was annealed at 65 °C for 5 min, cooled down to 25 °C at a rate of 0.58 °C·min^{-1}, and then allowed to equilibrate at 25 °C for 2 h to yield duplex F_1Q_1.

Preparation of riboswitches rS_1, rS_2, and rS_3. Taking rS_1 as an example, the corresponding cDNA was commercially synthesized and cloned into the PCR-linearized pET-23a vector between the T7

promoter and T7 terminator. The plasmid DNA was extracted and purified using a commercial kit per the manufacturer's instructions, and then used as templates for *in vitro* transcription (IVT). The IVT reaction was supplemented with equimolar amounts of ATP, UTP, CTP, and GTP, along with T7 RNA polymerase to drive transcription. The reaction mixture was incubated at 37 °C for 4 h to generate the target RNA transcripts. Subsequently, the crude RNA products were purified using VAHTS RNA Clean Beads following the manufacturer's recommended protocol.

Probing the conversion of L_i concentrations into discrete transcriptional states mediated by threshold-gated incoherent feedforward networks (TIFFNs).

For TIFFN-I-based system, a mixture containing A_1A_1' (0.04 μM), B_1B_1' (0.04 μM), D (0.04 μM), T_1 (0.04 μM), T_2 (0.04 μM), F_2Q_2 (0.20 μM), F_3Q_3 (0.20 μM), each NTP (2.86 mM), and T7 RNAP (0.48 $U \cdot \mu L^{-1}$) was prepared in 1× rCutSmart buffer. Aliquots (50 μL) of the reaction mixture were treated with varying volumes of L_i solution (1.00 μM in 1× rCutSmart buffer: 0, 1.0, 1.6, 3.0, 4.4, and 5.0 μL). Each reaction was then adjusted to a final volume of 100 μL using 1× rCutSmart buffer. Subsequently, the time-dependent fluorescence changes of the samples were monitored in real-time using a Cary Eclipse fluorescence spectrophotometer at 37 °C.

For TIFFN-II-based system, a mixture containing A_1 (0.04 μM), B_2' (0.04 μM), B_1B_2' (0.04 μM), C_1C_2' (0.04 μM), D (0.04 μM), T_1 (0.04 μM), T_2 (0.04 μM), T_3 (0.04 μM), F_2Q_2 (0.20 μM), F_3Q_3 (0.20 μM), each NTP (2.86 mM), and T7 RNAP (0.48 $U \cdot \mu L^{-1}$) was prepared in 1× rCutSmart buffer. Aliquots (50 μL) of the reaction mixture were treated with varying volumes of L_i solution (1.00 μM in 1× rCutSmart buffer: 0, 1.6, 2.5, 3.2, 4.0, 6.0, and 7.0 μL). Each reaction was then adjusted to a final volume of 100 μL using 1× rCutSmart buffer. Subsequently, the time-dependent fluorescence changes of the samples were monitored in real-time using a Cary Eclipse fluorescence spectrophotometer at 37 °C.

For TIFFN-III-based system, a mixture containing A_1A_1' (0.04 μM), B_1B_1' (0.04 μM), C_1C_1' (0.04 μM), D (0.04 μM), T_1 (0.04 μM), T_2 (0.04 μM), T_4 (0.04 μM), F_2Q_2 (0.20 μM), F_3Q_3 (0.20 μM), F_4Q_4 (0.20 μM), each NTP (2.86 mM), and T7 RNAP (0.48 $U \cdot \mu L^{-1}$) was prepared in 1× rCutSmart buffer. Aliquots (50 μL) of the reaction mixture were treated with varying volumes of L_i solution (1.00 μM in 1× rCutSmart buffer: 0, 1.0, 1.6, 3.0, 4.4, 6.0, 8.0, and 11.0 μL). Each reaction was then adjusted to a final volume of 100 μL using 1× rCutSmart buffer. Subsequently, the time-dependent fluorescence changes of the samples were monitored in real-time using a Cary Eclipse fluorescence spectrophotometer at 37 °C.

Probing the decoding of light duration into discrete transcriptional states dictated by photochemical-integration programmable duration-decoding systems (piPDDSs).

For piPDDS-I, a mixture containing L_iL_i' (0.10 μM), A_1A_1' (0.02 μM), B_1B_1' (0.02 μM), D (0.02 μM), T_1 (0.02 μM), T_2 (0.02 μM), F_2Q_2 (0.10 μM), F_3Q_3 (0.10 μM), each NTP (1.43 mM), and T7 RNAP (0.24 $U \cdot \mu L^{-1}$) was prepared in 1× rCutSmart buffer. Aliquots (100 μL) of the reaction mixture were irradiated with UV light (365 nm, 3 $mW \cdot cm^{-2}$) for varying durations (0, 0.8, 1.6, 2.5, 3.0, and 4.0 min). Subsequently, the time-dependent fluorescence changes of the samples were monitored in real-time using a Cary Eclipse fluorescence spectrophotometer at 37 °C.

For piPDDS-II, a mixture containing L_iL_i' (0.10 μM), A_1 (0.02 μM), B_2' (0.02 μM), B_1B_2' (0.02 μM), C_1C_2' (0.02 μM), D (0.02 μM), T_1 (0.02 μM), T_2 (0.02 μM), T_3 (0.02 μM), F_2Q_2 (0.10 μM), F_3Q_3 (0.10 μM), each NTP (1.43 mM), and T7 RNAP (0.24 $U \cdot \mu L^{-1}$) was prepared in 1× rCutSmart buffer. Aliquots (100 μL) of the reaction mixture were irradiated with UV light (365 nm, 3 $mW \cdot cm^{-2}$) for varying durations (0, 1.6, 2.5, 3.0, 4.0, 5.0, and 6.0 min). Subsequently, the time-dependent fluorescence changes of the samples were monitored in real-time using a Cary Eclipse fluorescence spectrophotometer at 37 °C.

For piPDDS-III, a mixture containing L_iL_i' (0.20 μM), A_1A_1' (0.02 μM), B_1B_1' (0.02 μM), C_1C_1' (0.02 μM), D (0.02 μM), T_1 (0.02 μM), T_2 (0.02 μM), T_4 (0.02 μM), F_2Q_2 (0.10 μM), F_3Q_3 (0.10 μM), F_4Q_4 (0.10 μM), each NTP (1.43 mM), and T7 RNAP (0.24 $U \cdot \mu L^{-1}$) was prepared in 1× rCutSmart buffer. Aliquots (100 μL) of the reaction mixture were irradiated with UV light (365 nm, 3 $mW \cdot cm^{-2}$) for varying durations (0, 0.8, 1.6, 2.5, 3.0, 4.0, 6.0, and 8.0 min). Subsequently, the time-dependent fluorescence changes of the samples were monitored in real-time using a Cary Eclipse fluorescence spectrophotometer at 37 °C.

Probing the persistence-selective of RNA inputs into discrete transcriptional states governed by a dissipative-filtering programmable duration-decoding system (dfPDDS).

For L_fL_f' reservoir with a low concentration, a mixture containing L_fL_f' (0.20 μM), A_1A_1' (0.25 μM), B_1B_1' (0.25 μM), D (0.25 μM), T_5 (0.25 μM), T_6 (0.25 μM), MG (16.40 μM), TO-1 (5.40 μM), each NTP (2.86 mM), T7 RNAP (10.70 $U \cdot \mu L^{-1}$), and RNase H (26.00 $U \cdot \mu L^{-1}$) was prepared in 1× rCutSmart buffer, yielding system dfPDDS-I with a low concentration of L_fL_f'. Aliquots (50 μL) of the reaction mixture were treated with varying volumes of rI solution (5.00 μM in 1× rCutSmart buffer: 1.0, 2.0, 4.0, 10.0, and 30.0 μL). Each reaction was then adjusted to a final volume of 100 μL using 1× rCutSmart buffer. Subsequently, the time-dependent fluorescence changes of the samples were monitored in real-time using a Cary Eclipse fluorescence spectrophotometer at 37 °C.

For L_fL_f' reservoir with a high concentration, a mixture containing L_fL_f' (1.25 μM), A_1A_1' (0.25 μM), B_1B_1' (0.25 μM), D (0.25 μM), T_5 (0.25 μM), T_6 (0.25 μM), MG (16.40 μM), TO-1 (5.40 μM), each NTP (2.86 mM), T7 RNAP (10.70 $U \cdot \mu L^{-1}$), and RNase H (80.00 $U \cdot \mu L^{-1}$) was prepared in 1× rCutSmart buffer, yielding system dfPDDS-I with a high concentration of L_fL_f'. Aliquots (50 μL) of the reaction mixture were treated with varying volumes of rI solution in 1× rCutSmart buffer (1.0 and 2.5 μL of 10 μM rI solution and 1.0, 2.0, 4.0, 10.0 and 30.0 μL of 31.25 μM rI solution). Each reaction was then adjusted to a final volume of 100 μL using 1× rCutSmart buffer. Subsequently, the time-dependent fluorescence changes of the samples were monitored in real-time using a Cary Eclipse fluorescence spectrophotometer at 37 °C.

Probing the decoding of light duration into discrete protein-output states dictated by the integrated piPDDS/riboswitch architectures.

For windowed activation of GFP synthesis, a mixture containing L_iL_i' (0.40 μM), A_1A_1' (0.08 μM), B_1B_1' (0.08 μM), D (0.08 μM), T_1 (0.08 μM), T_2 (0.08 μM), and RNase inhibitor (0.80 $U \cdot \mu L^{-1}$), together with PURExpress supplemented with 500 $ng \cdot \mu L^{-1}$ rS_1, was prepared, yielding the integrated piPDDS-I/GFP-regulating riboswitch architecture. Aliquots (100 μL) of the reaction mixture were irradiated with UV light (365 nm, 3 $mW \cdot cm^{-2}$) for varying durations (0, 0.8, 1.6, 2.5, 3.0, and 4.0 min). Subsequently, the time-dependent fluorescence changes of the samples were monitored in real-time using a Cary Eclipse fluorescence spectrophotometer at 37 °C.

For windowed repression of GFP synthesis, a mixture containing L_iL_i' (0.40 μM), A_1 (0.08 μM), B_1B_2' (0.08 μM), B_2' (0.08 μM), C_1C_2' (0.08 μM), D (0.08 μM), T_1 (0.08 μM), T_2 (0.08 μM), T_3 (0.08 μM), and RNase inhibitor (0.80 $U \cdot \mu L^{-1}$), together with PURExpress supplemented with 500 $ng \cdot \mu L^{-1}$ rS_1, was prepared, yielding the integrated piPDDS-II/GFP-regulating riboswitch architecture. Aliquots (100 μL) of the reaction mixture were irradiated with UV light (365 nm, 3 $mW \cdot cm^{-2}$) for varying durations (0, 1.6, 2.5, 3.0, 4.5, 5.0, and 6.0 min). Subsequently, the time-dependent fluorescence changes of the samples were monitored in real-time using a Cary Eclipse fluorescence spectrophotometer at 37 °C.

For multistate progression of protein synthesis, a mixture containing L_iL_i' (0.80 μM), A_1A_1' (0.08 μM), B_1B_1' (0.08 μM), C_1C_1' (0.08 μM), D (0.08 μM), T_1 (0.08 μM), T_2 (0.08 μM), T_4 (0.08 μM), and RNase inhibitor (0.80 $U \cdot \mu L^{-1}$), together with PURExpress supplemented with 500 $ng \cdot \mu L^{-1}$ rS_1 and 600 $ng \cdot \mu L^{-1}$ rS_2, was prepared, yielding the integrated piPDDS-III/GFP- and mCherry-regulating riboswitch architecture. Aliquots (100 μL) of the reaction mixture were irradiated with UV light (365 nm, 3 $mW \cdot cm^{-2}$) for varying durations (0, 0.8, 1.6, 2.5, 3.0, 4.0, 6.0, and 8.0 min). Subsequently, the

time-dependent fluorescence changes of the samples were monitored in real-time using a Cary Eclipse fluorescence spectrophotometer at 37 °C.

Probing L_i-concentration-dependent RNA-output-state selections in synthetic cells.

For TIFFN-I-based synthetic cells, the GUV assays were prepared following the aforementioned procedures, with the exception of the inner solution, which contained 300 mM sucrose, 10 mM Mg^{2+}, A_1A_1' (0.08 μM), B_1B_1' (0.08 μM), D (0.08 μM), T_1 (0.08 μM), T_2 (0.08 μM), F_2Q_2 (1.00 μM), F_3Q_3 (1.00 μM), each NTP (5.72 mM), T7 RNAP (0.95 $U\cdot\mu L^{-1}$), and input L_i at varying concentrations (0, 0.032, 0.064, 0.120, 0.176, and 0.200 μM). The prepared GUVs were then incubated at 37 °C to initiate internal transcription. After 2 h, fluorescence images were acquired using a Zeiss Axio Scope A1 microscope and analysed using ImageJ.

For TIFFN-II-based synthetic cells, the GUV assays were prepared following the aforementioned procedures, with the exception of the inner solution, which contained 300 mM sucrose, 10 mM Mg^{2+}, A_1 (0.08 μM), B_1B_2' (0.08 μM), B_2' (0.08 μM), C_1C_2' (0.08 μM), D (0.08 μM), T_1 (0.08 μM), T_2 (0.08 μM), T_3 (0.08 μM), F_2Q_2 (1.00 μM), F_3Q_3 (1.00 μM), each NTP (5.72 mM), T7 RNAP (0.95 $U\cdot\mu L^{-1}$), and input L_i at varying concentrations (0, 0.064, 0.100, 0.128, 0.160, 0.240, and 0.280 μM). The prepared GUVs were then incubated at 37 °C to initiate internal transcription. After 2 h, fluorescence images were captured via a Zeiss Axio Scope A1 microscope and processed with ImageJ.

For TIFFN-III-based synthetic cells, the GUV assays were prepared following the aforementioned procedures, with the exception of the inner solution, which contained 300 mM sucrose, 10 mM Mg^{2+}, A_1A_1' (0.08 μM), B_1B_1' (0.08 μM), C_1C_1' (0.08 μM), D (0.08 μM), T_1 (0.08 μM), T_2 (0.08 μM), T_4 (0.08 μM), F_2Q_2 (1.00 μM), F_3Q_3 (1.00 μM), F_4Q_4 (1.00 μM), each NTP (5.72 mM), T7 RNAP (0.95 $U\cdot\mu L^{-1}$), and input L_i at varying concentrations (0, 0.040, 0.064, 0.120, 0.176, 0.240, 0.320, and 0.440 μM). The prepared GUVs were then incubated at 37 °C to initiate internal transcription. After 2 h, fluorescence images were acquired using a Zeiss Axio Scope A1 microscope and analysed using ImageJ.

Fluorescence data processing

To facilitate comparison of fluorescence responses across different experimental conditions, the fluorescence intensities were normalised to a 0–1 range using the following formula:

$$\text{Norm. Fluor.} = \frac{\left(F_t - F_{min}\right)}{\left(F_{max} - F_{min}\right)}$$

where F_t denotes the fluorescence intensity of a sample measured at time t (t = 180 min for transcription;

t = 500 min for translation), F_{min} and F_{max} represent the minimal and maximum fluorescence intensities of the corresponding output among all samples, respectively.

To quantify fluorescence signals associated with transcription, protein synthesis and cargo release in synthetic cells, relative fluorescence intensities were calculated using the following formula:

$$\text{Norm. Fluor.} = \frac{F}{F_{max}}$$

where F represents the fluorescence intensity of a given sample, and F_{max} is the maximum fluorescence intensity of the corresponding output among all samples. Fluorescence intensities for confocal images were quantified using ImageJ software.

2. Design Principles of The Programmable Duration-Decoding Framework

To fulfill the decoding of stimulus duration into distinct functional states, the nucleic-acid sequences within the programmable duration-decoding framework were designed by using NUPACK software.

i) Design of piPDDS-I shown in Fig. 2b and Supplementary Fig. 10a. In the input-transduction module with photochemical integration, we designed a photocleavable duplex L_iL_i' where strand L_i' incorporates four photocleavable (PC) linkers while L_i functions as a readable DNA signal for downstream processing. Under fixed irradiance, continued illumination progressively cleaves L_i', thus destabilizing duplex L_iL_i' and releasing L_i in a duration-dependent manner. We developed TIFFN-I as the molecular decision-making layer, in which two different threshold-gated strand-displacement reactions were designed to partition L_i concentration spectrum into two specific ranges. The corresponding reactions are as follows: $L_i + A_1A_1' \leftrightarrow L_iA_1' + A_1$; $L_i + B_1B_1' \leftrightarrow L_iB_1' + B_1$. Each reaction generates a specific signalling strand that was engineered to trigger D-mediated competitive reactions for transcription actuation. The relevant reactions are as follows: $A_1 + D + T_1 \leftrightarrow A_1DT_1$; $B_1 + A_1DT_1 + T_2 \leftrightarrow B_1DT_2 + A_1T_1$. T_1 and T_2, nicked T7 promoters, can be activated by A_1D and B_1D via suppling a promoter-completing strand to the incomplete T7 promoter, driving rP_1 and rP_2 transcription, respectively. The resulting RNA products, rP_1 and rP_2, were quantified by strand displacement with their corresponding fluorophore-quencher reporters ($rP_1 + F_2Q_2 \leftrightarrow rP_1Q_2 + F_2$; $rP_2 + F_3Q_3 \leftrightarrow rP_2Q_3 + F_3$). Free energy values of L_i-induced threshold-gated strand-displacement reactions, the following competitive reactions, and the reporting reactions calculated based on the predicted free energy values of the structures by NUPACK software were as follows:

$L_i + L_i' \leftrightarrow L_iL_i'$, $\Delta G = -51.05$ kcal·mol^{-1};

$L_i + A_1A_1' \leftrightarrow L_iA_1' + A_1$, $\Delta G = -32.94$ kcal·mol^{-1};

$L_i + B_1B_1' \leftrightarrow L_iB_1' + B_1$, $\Delta G = -15.46$ kcal·mol^{-1};

$A_1 + D + T_1 \leftrightarrow A_1DT_1$, $\Delta G = -30.89$ kcal·mol^{-1};

$B_1 + A_1DT_1 + T_2 \leftrightarrow B_1DT_2 + A_1T_1$, $\Delta G = -17.54$ kcal·mol^{-1};

$rP_1 + F_2Q_2 \leftrightarrow rP_1Q_2 + F_2$, $\Delta G = -8.19$ kcal·mol^{-1};

$rP_2 + F_3Q_3 \leftrightarrow rP_2Q_3 + F_3$, $\Delta G = -6.71$ kcal·mol^{-1}.

ii) Design of piPDDS-II shown in Fig. 2d and Supplementary Fig. 11a. In the input-transduction module with photochemical integration, we designed a photocleavable duplex L_iL_i' where strand L_i' incorporates four PC linkers while L_i functions as a readable DNA signal for downstream processing. Under fixed irradiance, continued illumination progressively cleaves L_i', thus destabilizing duplex L_iL_i' and releasing L_i in a duration-dependent manner. We developed TIFFN-II as the molecular decision-making layer, in which three different threshold-gated strand-displacement reactions were designed to partition L_i concentration spectrum into three specific ranges. The corresponding reactions are as follows: $L_i + B_2' \leftrightarrow L_iB_2'$; $L_i + B_1B_2' \leftrightarrow L_iB_2' + B_1$; $L_i + C_1C_2' \leftrightarrow L_iC_2' + C_1$. In this system, preformed

A_1D engages transcriptional module T_1 to assemble A_1DT_1, thereby presetting the system in an rP_1-ON state. The last two threshold-gated reaction generates a specific signalling strand that was engineered to trigger D-mediated competitive reactions for transcription actuation. The relevant reactions are as follows: $B_1 + A_1DT_1 + T_2 \leftrightarrow B_1DT_2 + A_1T_1$; $C_1 + B_1DT_2 + T_3 \leftrightarrow C_1DT_3 + B_1T_2$. Structures B_1DT_2 and C_1DT_3 were engineered to drive rP_2 and rP_1 transcription, respectively. The resulting RNA products, rP_1 and rP_2, were quantified by strand displacement with their corresponding fluorophore-quencher reporters ($rP_1 + F_2Q_2 \leftrightarrow rP_1Q_2 + F_2$; $rP_2 + F_3Q_3 \leftrightarrow rP_2Q_3 + F_3$). Free energy values of L_i-induced threshold-gated strand-displacement reactions, the following competitive reactions, and the reporting reactions calculated based on the predicted free energy values of the structures by NUPACK software were as follows:

$L_i + L_i' \leftrightarrow L_iL_i'$, $\Delta G = -48.73$ kcal·mol^{-1};

$L_i + B_2' \leftrightarrow L_iB_2'$, $\Delta G = -47.07$ kcal·mol^{-1};

$L_i + B_1B_2' \leftrightarrow L_iB_2' + B_1$, $\Delta G = -14.70$ kcal·mol^{-1};

$L_i + C_1C_2' \leftrightarrow L_iC_2' + C_1$, $\Delta G = -7.53$ kcal·mol^{-1};

$A_1 + D + T_1 \leftrightarrow A_1DT_1$, $\Delta G = -30.89$ kcal·mol^{-1};

$B_1 + A_1DT_1 + T_2 \leftrightarrow B_1DT_2 + A_1T_1$, $\Delta G = -17.54$ kcal·mol^{-1};

$C_1 + B_1DT_2 + T_3 \leftrightarrow C_1DT_3 + B_1T_2$, $\Delta G = -19.96$ kcal·mol^{-1};

$rP_1 + F_2Q_2 \leftrightarrow rP_1Q_2 + F_2$, $\Delta G = -8.19$ kcal·mol^{-1};

$rP_2 + F_3Q_3 \leftrightarrow rP_2Q_3 + F_3$, $\Delta G = -6.71$ kcal·mol^{-1}.

iii) Design of piPDDS-III shown in Fig. 2f and Supplementary Fig. 12a. In the input-transduction module with photochemical integration, we designed a photocleavable duplex L_iL_i' where strand L_i' incorporates four PC linkers while L_i functions as a readable DNA signal for downstream processing. Under fixed irradiance, continued illumination progressively cleaves L_i', thus destabilizing duplex L_iL_i' and releasing L_i in a duration-dependent manner. We developed TIFFN-III as the molecular decision-making layer, in which three different threshold-gated strand-displacement reactions were designed to partition L_i concentration spectrum into three specific ranges. The corresponding reactions are as follows: $L_i + A_1A_1' \leftrightarrow L_iA_1' + A_1$; $L_i + B_1B_1' \leftrightarrow L_iB_1' + B_1$; $L_i + C_1C_1' \leftrightarrow L_iC_1' + C_1$. Each reaction generates a specific signalling strand that was engineered to trigger D-mediated competitive reactions for transcription actuation. The relevant reactions are as follows: $A_1 + D + T_1 \leftrightarrow A_1DT_1$; $B_1 + A_1DT_1 + T_2 \leftrightarrow B_1DT_2 + A_1T_1$; $C_1 + B_1DT_2 + T_4 \leftrightarrow C_1DT_4 + B_1T_2$. Structures A_1DT_1, B_1DT_2, and C_1DT_4 were engineered to drive rP_1, rP_2, and rP_3 transcription, respectively. The resulting RNA products, rP_1, rP_2, and rP_3, were quantified by strand displacement with their corresponding fluorophore-quencher reporters ($rP_1 + F_2Q_2 \leftrightarrow rP_1Q_2 + F_2$; $rP_2 + F_3Q_3 \leftrightarrow rP_2Q_3 + F_3$; $rP_3 + F_4Q_4 \leftrightarrow rP_3Q_4 + F_4$). Free energy values of L_i-induced threshold-gated strand-displacement reactions, the following competitive

reactions, and the reporting reactions calculated based on the predicted free energy values of the structures by NUPACK software were as follows:

$L_i + L_i' \leftrightarrow L_iL_i'$, $\Delta G = -51.05$ kcal·mol^{-1};

$L_i + A_1A_1' \leftrightarrow L_iA_1' + A_1$, $\Delta G = -32.94$ kcal·mol^{-1};

$L_i + B_1B_1' \leftrightarrow L_iB_1' + B_1$, $\Delta G = -15.46$ kcal·mol^{-1};

$L_i + C_1C_1' \leftrightarrow L_iC_1' + C_1$, $\Delta G = -9.64$ kcal·mol^{-1};

$A_1 + D + T_1 \leftrightarrow A_1DT_1$, $\Delta G = -30.89$ kcal·mol^{-1};

$B_1 + A_1DT_1 + T_2 \leftrightarrow B_1DT_2 + A_1T_1$, $\Delta G = -17.54$ kcal·mol^{-1};

$C_1 + B_1DT_2 + T_4 \leftrightarrow C_1DT_4 + B_1T_2$, $\Delta G = -19.96$ kcal·mol^{-1};

$rP_1 + F_2Q_2 \leftrightarrow rP_1Q_2 + F_2$, $\Delta G = -8.19$ kcal·mol^{-1};

$rP_2 + F_3Q_3 \leftrightarrow rP_2Q_3 + F_3$, $\Delta G = -6.71$ kcal·mol^{-1};

$rP_3 + F_4Q_4 \leftrightarrow rP_3Q_4 + F_4$, $\Delta G = -7.55$ kcal·mol^{-1}.

iv) Design of dfPDDS-I shown in Fig. 3b and Supplementary Figs. 13 and 14. In the input-transduction module with dissipative filtering, we designed a threshold duplex L_fL_f' where L_f functions as a readable DNA signal for downstream processing. RNA input rI was engineered to react with L_fL_f' to form rIL_f' and release L_f, and subsequent RNase H-mediated degradation of rI within rIL_f' generates L_f' that recaptures free L_f to reform L_fL_f' ($rI + L_fL_f' \leftrightarrow rIL_f' + L_f$; $rIL_f' + \text{RNase H} \rightarrow L_f' + \text{rI fragments} + \text{RNase H}$; $L_f' + L_f \leftrightarrow L_fL_f'$). For rI with the same concentration, a larger L_fL_f' reservoir produces a higher-amplitude but shorter-lived L_f trajectory. By contrast, a smaller L_fL_f' reservoir yields a lower-amplitude but longer-lived L_f trajectory. We developed TIFFN-I as the molecular decision-making layer, in which two different threshold-gated strand-displacement reactions were designed to partition L_f concentration spectrum into two specific ranges. The corresponding reactions are as follows: $L_f + A_1A_1' \leftrightarrow L_fA_1' + A_1$; $L_f + B_1B_1' \leftrightarrow L_fB_1' + B_1$. Each reaction generates a specific signalling strand that was engineered to trigger D-mediated competitive reactions for transcription actuation. The relevant reactions are as follows: $A_1 + D + T_5 \leftrightarrow A_1DT_5$; $B_1 + A_1DT_5 + T_6 \leftrightarrow B_1DT_6 + A_1T_5$. Structures A_1DT_5 and B_1DT_6 were engineered to drive the transcription of Mango (MG) aptamer and TO1-3PEG-Biotin (TO-1) aptamer, respectively. Free energy values of L_f-induced threshold-gated strand-displacement reactions and the following competitive reactions calculated based on the predicted free energy values of the structures by NUPACK software were as follows:

$L_f + L_f' \leftrightarrow L_fL_f'$, $\Delta G = -58.77$ kcal·mol^{-1};

$rI + L_fL_f' \leftrightarrow rIL_f' + L_f$, $\Delta G = -17.07$ kcal·mol^{-1};

$L_f + A_1A_1' \leftrightarrow L_fA_1' + A_1$, $\Delta G = -31.36$ kcal·mol^{-1};

$L_f + B_1B_1' \leftrightarrow L_fB_1' + B_1$, $\Delta G = -15.41$ kcal·mol^{-1};

$A_1 + D + T_5 \leftrightarrow A_1DT_5$, $\Delta G = -30.88$ kcal·mol^{-1};

$B_1 + A_1DT_5 + T_6 \leftrightarrow B_1DT_6 + A_1T_5$, $\Delta G = -17.54$ kcal·mol^{-1}.

v) Design of the integrated piPDDS/riboswitch architectures shown in Figs. 5 and 6 and Supplementary Figs. 26−28. Riboswitches were engineered to consist of a ribosome-binding site (RBS)-sequestering hairpin and an expression platform that undergoes an RNA output-induced conformational change to regulate gene expression. However, these above RNA outputs were designed to activate their cognate, sequence-matched riboregulator by hybridizing with the engineered 5′ leader sequence of its target mRNA, thereby disrupting the hairpin that sequesters the RBS and enabling translation initiation. Specifically, rP_1 was designed to act as the RNA trigger for the green fluorescent protein (GFP)-regulating riboswitch module (rS_1) or the α-HL-regulating riboswitch module (rS_3); and rP_2 was designed to act as the RNA trigger for the mCherry-regulating riboswitch module (rS_2): $rP_1 + rS_1 \leftrightarrow rP_1rS_1$; $rP_1 + rS_3 \leftrightarrow rP_1rS_3$; $rP_2 + rS_2 \leftrightarrow rP_2rS_2$. The resulting structures rP_1rS_1, rP_1rS_3, and rP_2rS_2 were engineered to drive the synthesis of proteins GFP, α-HL, and mCherry, respectively. Free energy values of RNA output-induced reactions for conformational changes calculated based on the predicted free energy values of the structures by NUPACK software were as follows:

$rP_1 + rS_1 \leftrightarrow rP_1rS_1$, $\Delta G = -34.42$ kcal·mol^{-1};

$rP_2 + rS_2 \leftrightarrow rP_2rS_2$, $\Delta G = -34.64$ kcal·mol^{-1};

$rP_1 + rS_3 \leftrightarrow rP_1rS_3$, $\Delta G = -32.95$ kcal·mol^{-1}.

3. L_i-Concentration-Dependent RNA-Output-State Selections in Synthetic Cells

In order to establish L_i-to-RNA transfer functions that define how L_i concentration is resolved into programmable RNA-output states by TIFFN-mediated decision-making and transcriptional actuation, we decoupled photochemical L_i generation from the downstream decoding and actuation processes and directly supplied defined L_i concentrations to the integrated architecture of a TIFFN-I, TIFFN-II, or TIFFN-III layer with its corresponding transcriptional actuation layer.

i) Programming L_i concentration-dependent RNA-output-states. For the integrated architecture of TIFFN-I with its transcriptional actuation module as shown in Supplementary Fig. 3, neither rP_1 nor rP_2 transcription was detected in the absence of input L_i, indicating minimal formation of the corresponding transcriptionally active complexes, A_1DT_1 and B_1DT_2. Input L_i within the low concentration regime (<0.048 μM) selectively induced rP_1 transcription, consistent with A_1D-mediated assembly of the rP_1-active transcriptional complex, A_1DT_1. Input L_i beyond 0.013 μM shifted the system toward B_1D-mediated assembly of the rP_2-active transcriptional complex, B_1DT_2, suppressing rP_1 transcription and initiating rP_2 transcription. Thus, the TIFFN-I-based integrated architecture translates L_i concentration into a bounded transcriptional activation window, confining rP_1 transcription to the low concentration region of L_i while routing its increased concentration to the alternative rP_2 output. Furthermore, when adding extra A_1' (0.040 μM) in TIFFN-I, the rP_1-output window was postponed to the L_i-concentration regime of 0.033–0.068 μM (Supplementary Fig. 6), indicating the programmability of the location of the bounded transcriptional activation window. However, increasing the concentration of threshold duplex A_1A_1' from 0.020 to 0.060 μM in TIFFN-I, the rP_1-output window was extended to the L_i concentration regime of 0.005–0.079 μM (Supplementary Fig. 7), demonstrating the programmability of the size of the bounded transcriptional activation window. Thus, the location and size of the rP_1-output window can be programmed by tuning the TIFFN compositions.

For the integrated architecture of TIFFN-II with its transcriptional actuation module as shown in Supplementary Fig. 4, rP_1 transcription remained active while rP_2 remained inactive in the low L_i concentration regime (<0.016 μM), indicating that A_1DT_1 is the dominant transcriptional complex. In the intermediate L_i concentration regime (0.015–0.060 μM), the transcriptional output was redirected from rP_1 to rP_2, consistent with the replacement of A_1DT_1 by B_1DT_2 as the dominant transcriptional complex. In the high L_i concentration regime (>0.046 μM), rP_2 activation was terminated, and rP_1 transcription was restored, in accordance with the substitution of rP_1-active C_1DT_3 for rP_2-active B_1DT_2. This ON→OFF→ON behaviour of rP_1 demonstrates that reprogramming TIFFN topology from TIFFN-I to TIFFN-II can convert L_i-concentration decoding from a bounded transcriptional activation window into a bounded repression window of rP_1. Furthermore, when increasing B_2' concentration from 0.020 to 0.060 μM in TIFFN-II, the bounded transcriptional repression window of

rP_1 was postponed to the L_i concentration regime of 0.048–0.092 μM (Supplementary Fig. 8), indicating the programmability of the location of the bounded transcriptional activation window. However, when the concentration of threshold duplex B_1B_2' was increased from 0.020 to 0.060 μM in TIFFN-II, the bounded transcriptional repression window of rP_1 was extended to the L_i concentration regime of 0.021–0.086 μM (Supplementary Fig. 9), demonstrating the programmability of the size of the bounded transcriptional activation window. Thus, by tuning the TIFFN-II compositions, the location and size of the bounded transcriptional repression window of rP_1 can be programmed.

For the integrated architecture of TIFFN-III with its transcriptional actuation module as shown in Supplementary Fig. 5, no RNA output was detected in the absence of input L_i. As L_i concentration increased, transcription progressed stepwise from rP_1 to rP_2 and then to rP_3, with each RNA output selectively produced within its preassigned L_i concentration regime (<0.053 μM, 0.016–0.090 μM, and >0.049 μM, respectively). Together, these results demonstrate that TIFFN-III extends L_i-concentration decoding beyond bounded windows, partitioning a continuous concentration of L_i into a sequential progression of RNA outputs ($rP_1 \rightarrow rP_2 \rightarrow rP_3$).

ii) L_i concentration-dependent RNA-output-state selections in synthetic cells. Next, we investigated whether the concentration-decoding logic established in solution could be transferred into synthetic cells and used to program distinct RNA output states. To this end, the integrated architecture of a TIFFN-mediated decision-making layer and a transcriptional layer was encapsulated into GUVs. The generated RNA outputs were detected through strand displacement reactions using corresponding fluorophore-quencher reporter probes and quantitatively characterised by single-vesicle fluorescence imaging and population-averaged fluorescence analysis.

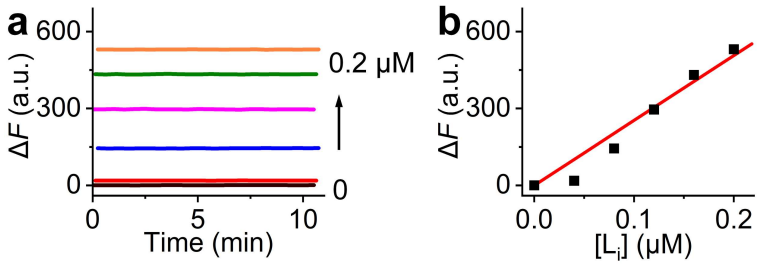
In TIFFN-I-based synthetic cells (Supplementary Fig. 18), negligible RNA reporter fluorescence was observed in the absence of L_i input, indicating that the system remained in an OFF state. Upon treatment with L_i, rP_1-associated reporter fluorescence appeared within a low L_i concentration regime (<0.150 μM), whereas increased L_i concentration (>0.080 μM) produced rP_2-associated reporter fluorescence. These results demonstrate that, after compartmentalisation, the TIFFN-I-based synthetic cells preserve L_i concentration-decoding activity, with rP_1 transcription confined within a bounded L_i concentration regime.

In TIFFN-II-based synthetic cells (Supplementary Fig. 19), rP_1-associated fluorescence was predominantly observed in GUVs at the low L_i concentration regime (<0.064 μM), whereas rP_2 output remained inactive, indicating an rP_1-dominated transcriptional state. Upon increasing L_i concentration to the intermediate regime (0.064–0.207 μM), rP_2-associated reporter fluorescence increased as rP_1-associated reporter fluorescence decreased, indicating that the transcriptional output was redirected from rP_1 to rP_2. At the high L_i concentration regime (>0.207 μM), rP_1-associated fluorescence became dominant again while rP_2-associated reporter fluorescence disappeared, demonstrating the restoration

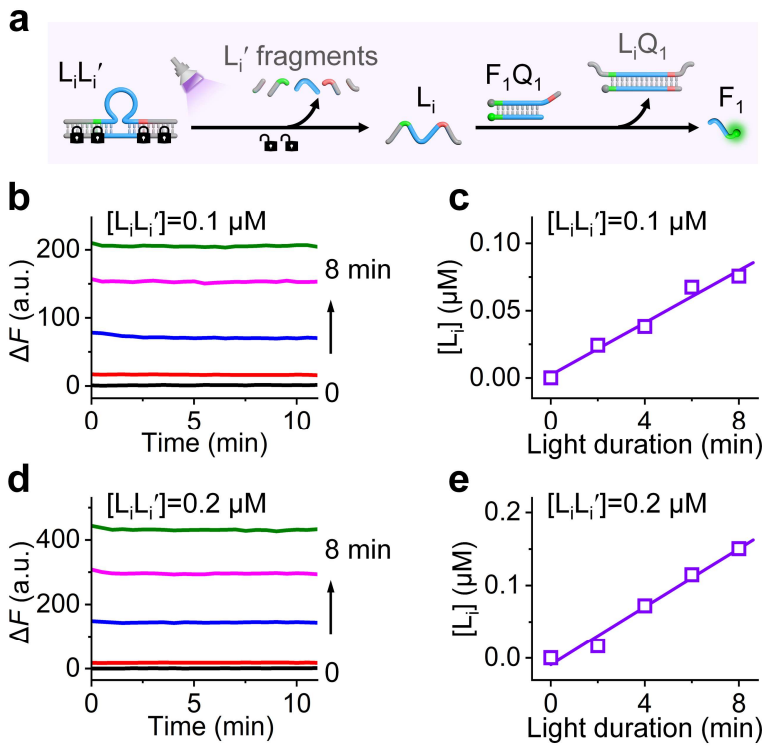
of rP_1 transcription. These results demonstrate that the TIFFN-II-based synthetic cells generate a L_i concentration-dependent repression of rP_1 transcription.

In TIFFN-III-based synthetic cells(Supplementary Fig. 20), rP_1-associated fluorescence was observed in GUVs within the low L_i concentration regime (<0.126 μM). Within the intermediate L_i concentration regime (0.064–0.264 μM), rP_2-associated fluorescence emerged as rP_1-associated fluorescence decreased. Within the high L_i concentration regime (>0.247 μM), rP_3-associated reporter fluorescence emerged as rP_2-associated reporter fluorescence decreased. These results demonstrate that the TIFFN-III-based synthetic cells convert L_i concentration into a sequential $rP_1 \rightarrow rP_2 \rightarrow rP_3$ RNA output progression.

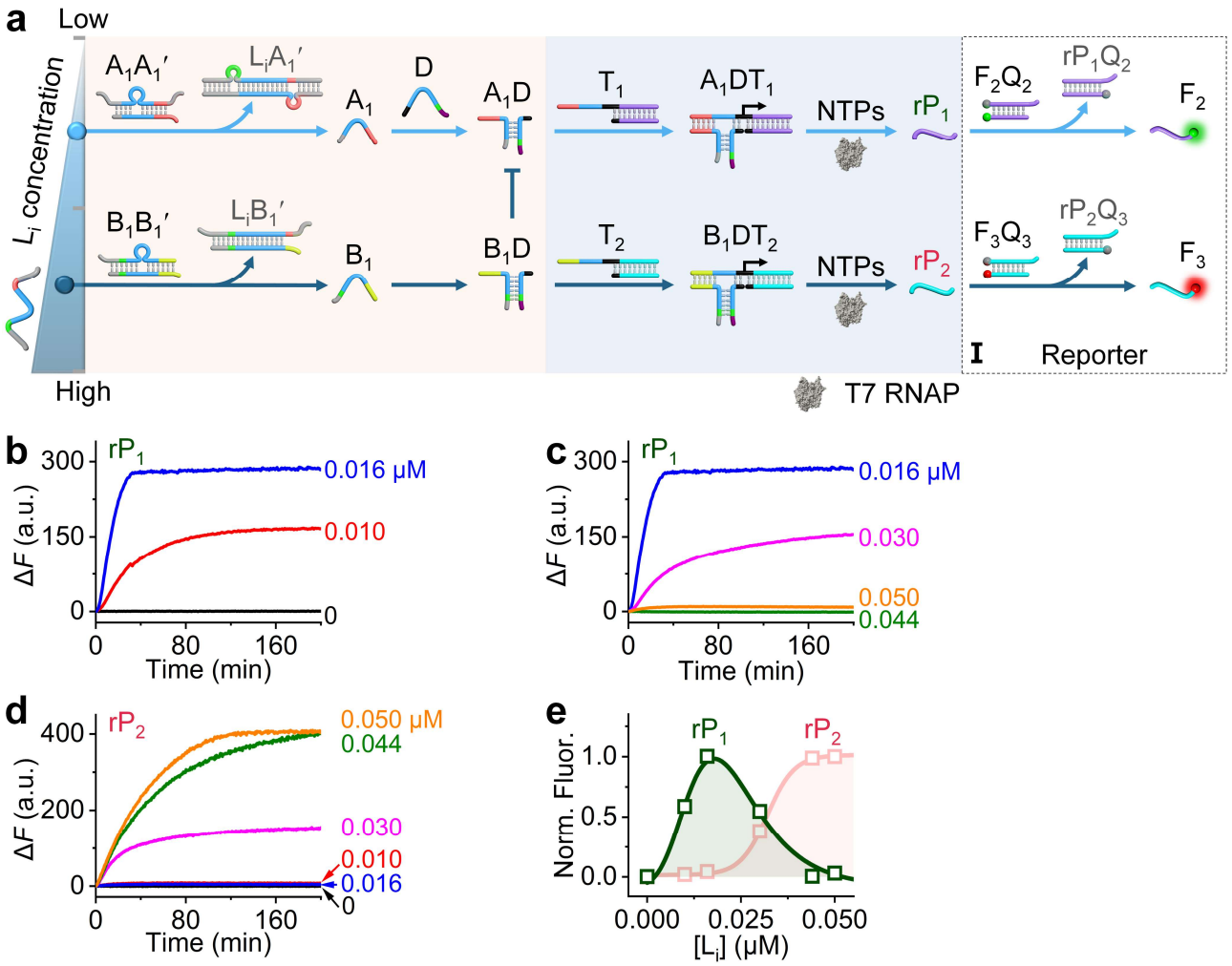
4. Characterisations of PDDS-Dictated Decoding of Stimulus Duration into Discrete Transcriptional States



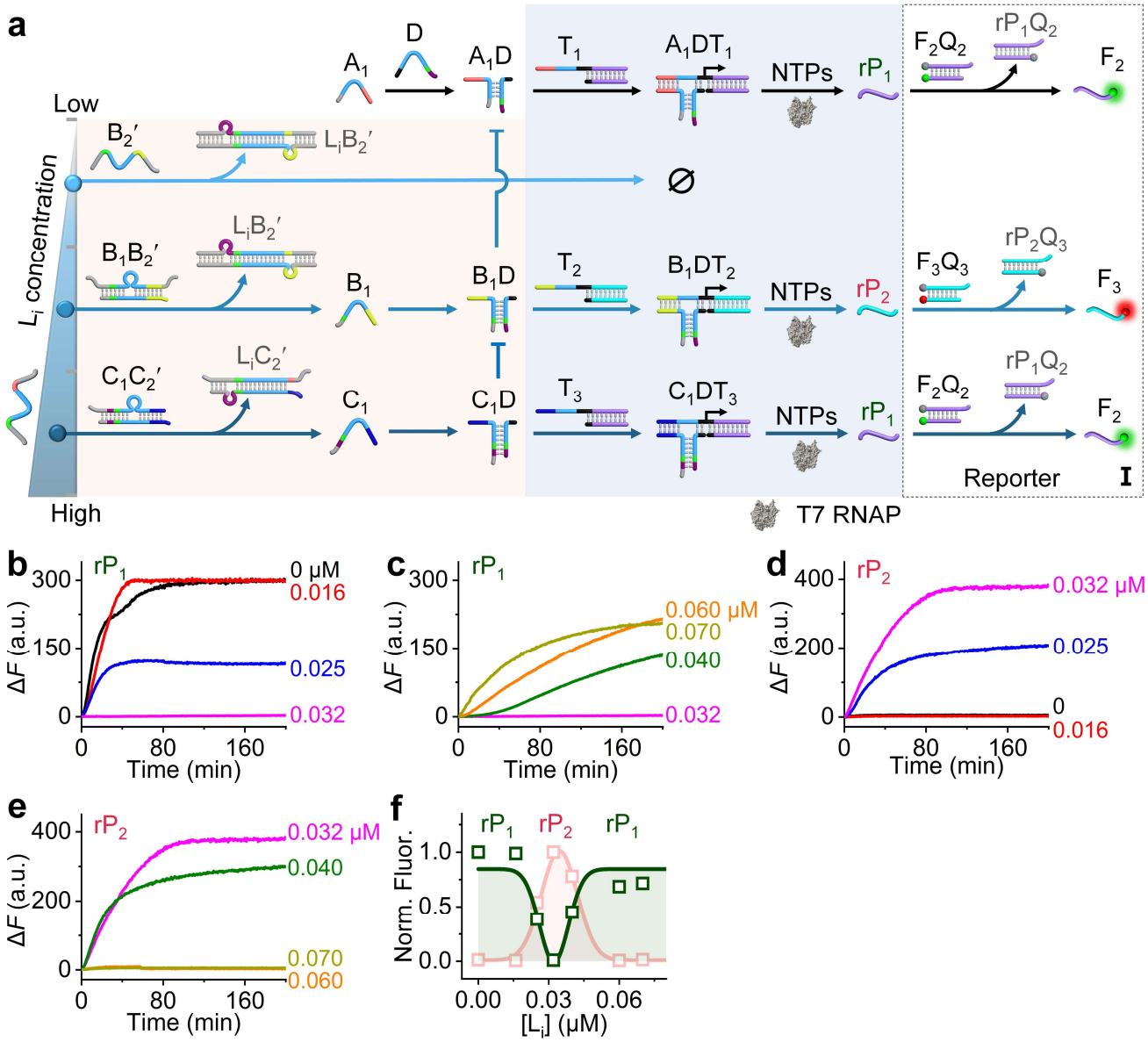
Supplementary Fig. 1 | Calibration curve of L_i. a, Time-dependent changes in FAM fluorescence reporting free L_i at various concentrations: 0, 0.04, 0.08, 0.12, 0.16, and 0.20 μM, in the presence of 0.20 μM F_1Q_1. **b**, Corresponding calibration curve of FAM fluorescence (λ_{em} = 516 nm) as a function of L_i concentration, derived from the results shown in **a**.



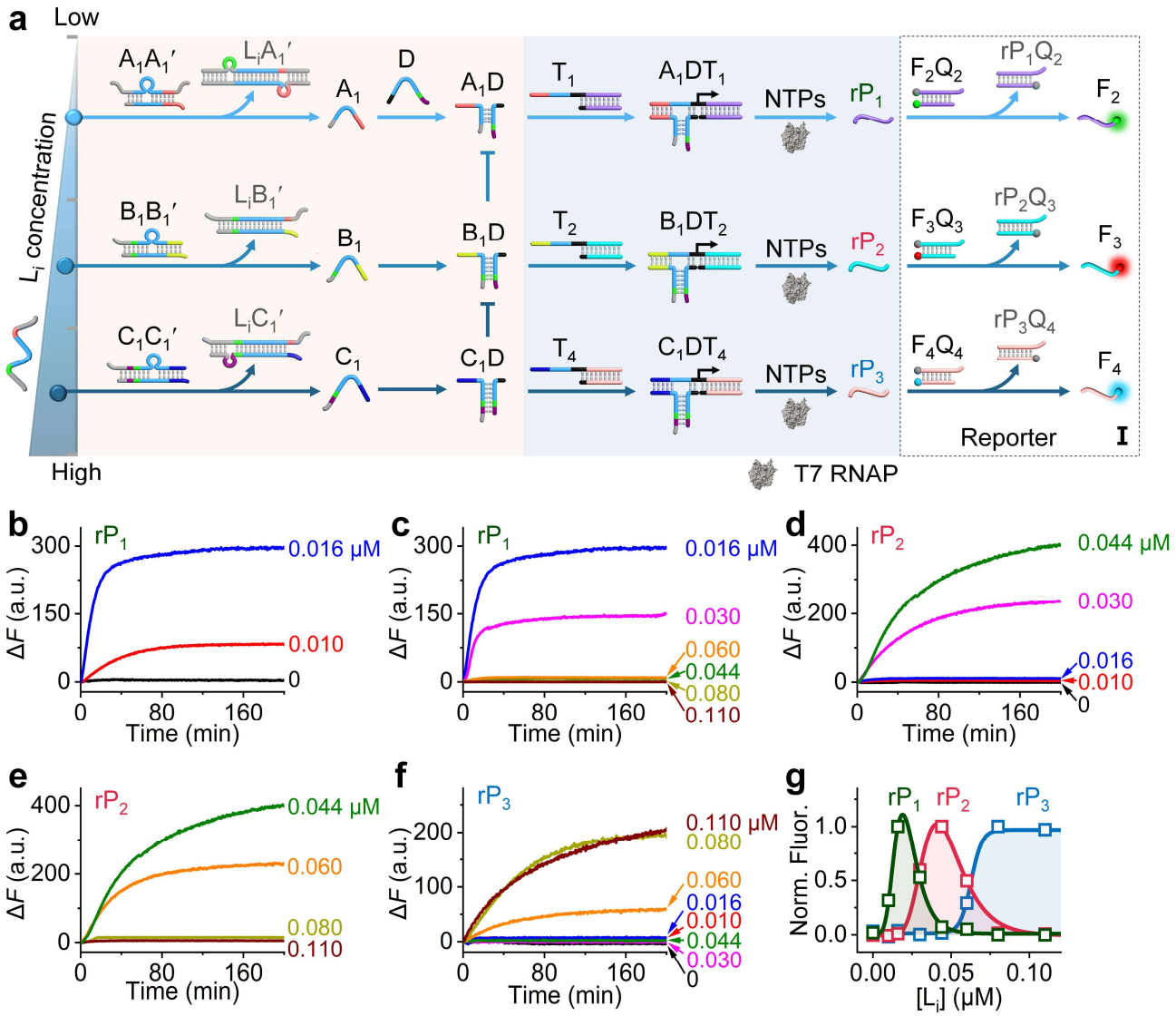
Supplementary Fig. 2 | Calibration curves of the released L_i under UV irradiation. a, Schematic showing the release of L_i from L_iL_i' upon UV irradiation and its detection by strand-displacement reactions using fluorescent reporter F_1Q_1. **b**,**d**, Time-dependent changes in FAM fluorescence (λ_{em} = 516 nm) reporting L_i release upon irradiating the L_iL_i'/F_1Q_1 mixtures with UV light for varying durations (0, 2, 4, 6, and 8 min), in the presence of 0.1 μM L_iL_i' (**b**) and 0.2 μM L_iL_i' (**d**). **c**,**e**, Corresponding L_i concentration as a function of light duration, calculated from the fluorescence intensities at 10 min shown in **b** and **d** using the calibration curve established in Supplementary Fig. 1.



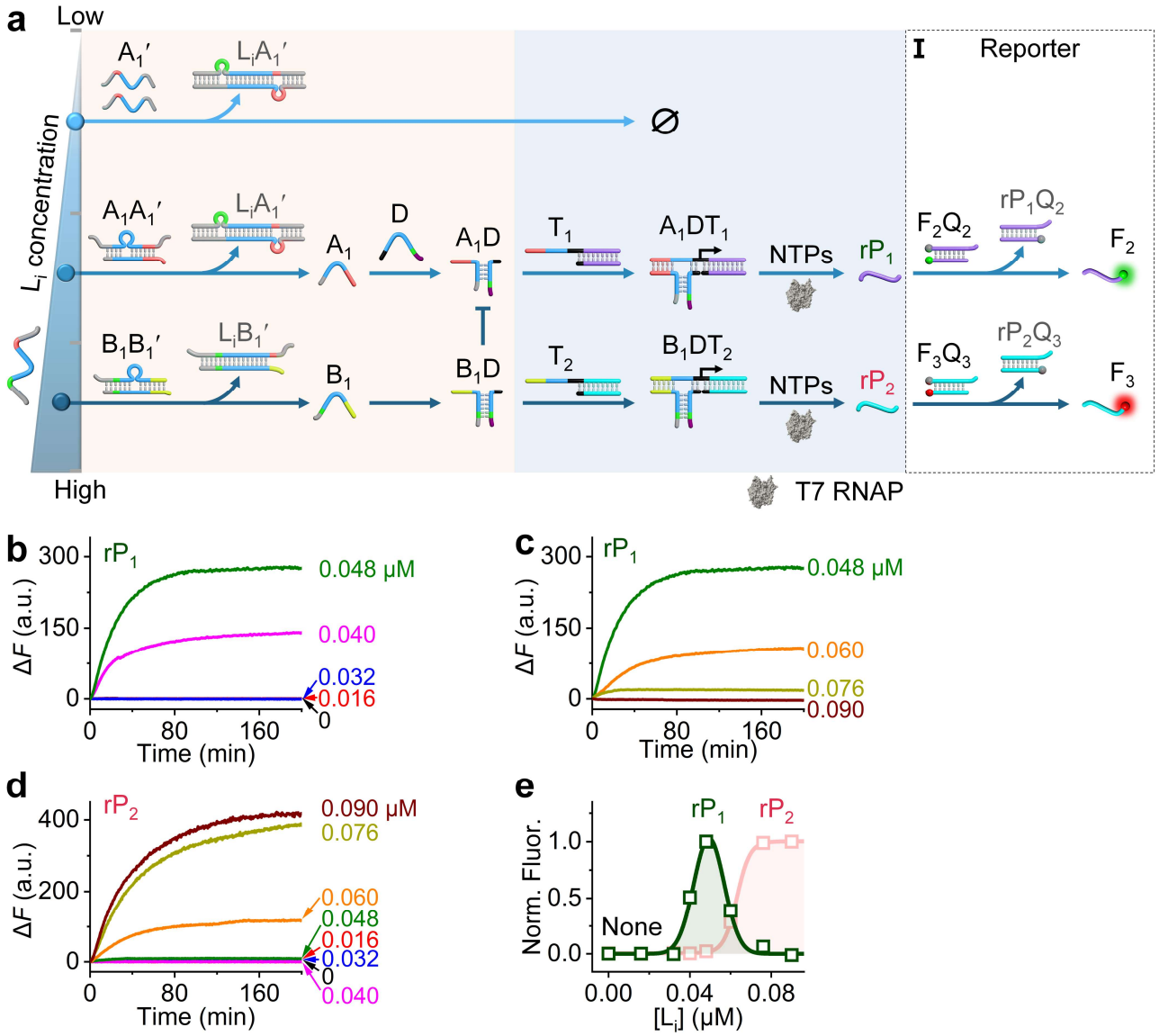
Supplementary Fig. 3 | TIFFN-I-dictated decoding of L_i concentration into discrete transcriptional states. a, Schematic illustrating the operation of the integrated architecture of TIFFN-I with its transcriptional actuation module, which converts increasing L_i concentration into discrete transcriptional states corresponding to rP_1 and rP_2 outputs. Panel I—Schematic of RNA output detection via strand-displacement reactions using corresponding fluorescent reporters. **b**,**c**, Time-dependent fluorescence changes of FAM reporting rP_1 transcription upon subjecting the integrated architecture to different concentrations of L_i: 0, 0.010, and 0.016 μM (**b**); 0.016, 0.030, 0.044, and 0.050 μM (**c**). **d**, Time-dependent fluorescence changes of ROX reporting rP_2 transcription upon subjecting the integrated architecture to different concentrations of L_i: 0, 0.010, 0.016, 0.030, 0.044, and 0.050 μM. **e**, Normalised fluorescence responses as a function of L_i concentration, derived from the results shown in **b**–**d**.



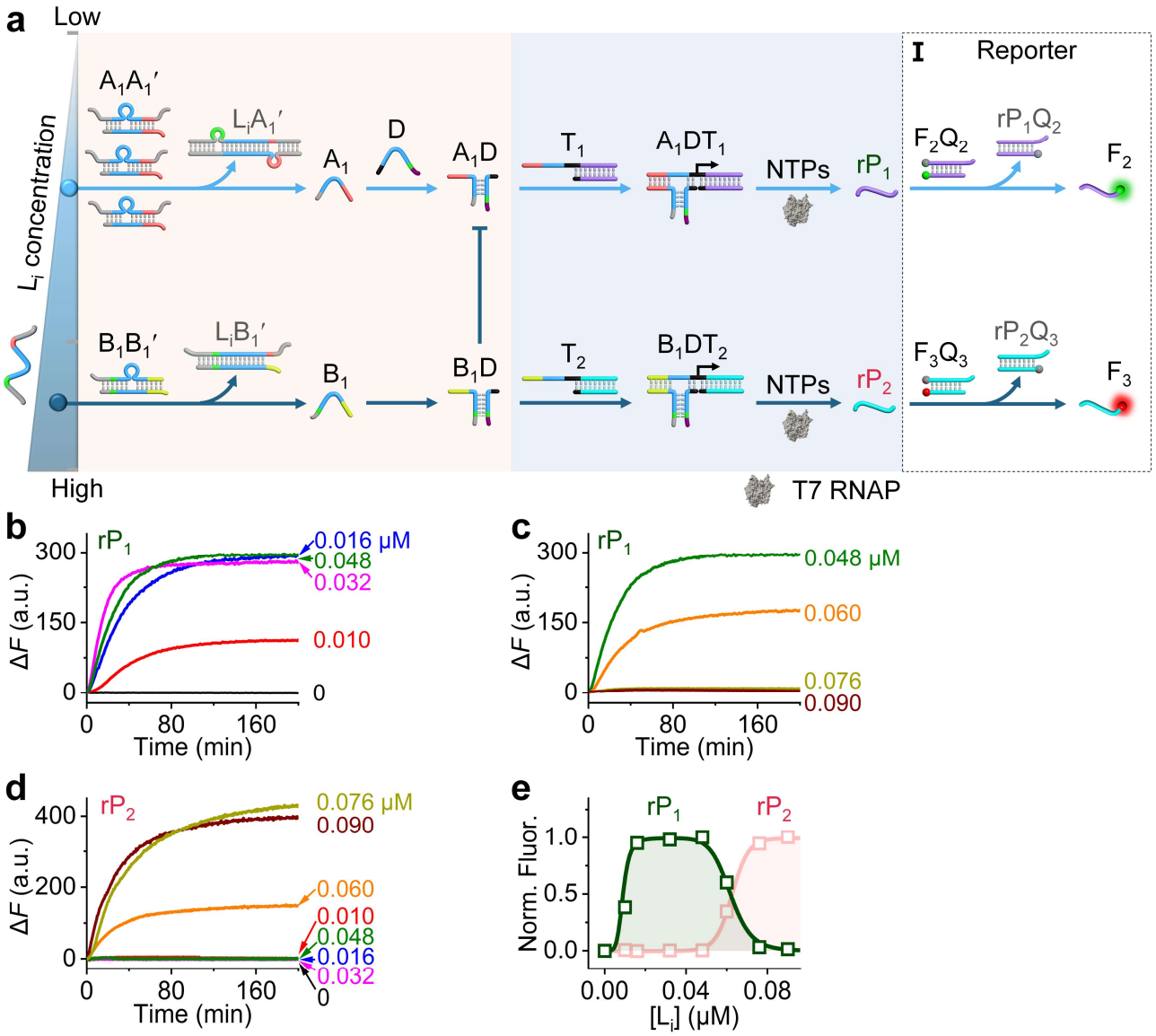
Supplementary Fig. 4 | TIFFN-II-dictated decoding of L_i concentration into discrete transcriptional states. a, Schematic showing the operation of the integrated architecture of TIFFN-II with its corresponding transcriptional actuation module, which converts increasing L_i concentration into discrete transcriptional states corresponding to rP_1, rP_2, and rP_1 outputs. Panel I—Schematic of RNA product detection via strand-displacement reactions using corresponding fluorescent reporters. **b**,**c**, Time-dependent changes in FAM fluorescence reporting rP_1 transcription upon subjecting the integrated architecture to different concentrations of L_i: 0, 0.016, 0.025, and 0.032 μM (**b**); 0.032, 0.040, 0.060, and 0.070 μM (**c**). **d**,**e**, Time-dependent changes in ROX fluorescence reporting rP_2 transcription upon subjecting the integrated architecture to different concentrations of L_i: 0, 0.016, 0.025, and 0.032 μM (**d**); 0.032, 0.040, 0.060, and 0.070 μM (**e**). **f**, Normalised fluorescence responses as a function of L_i concentration, derived from the results shown in **b**–**e**.



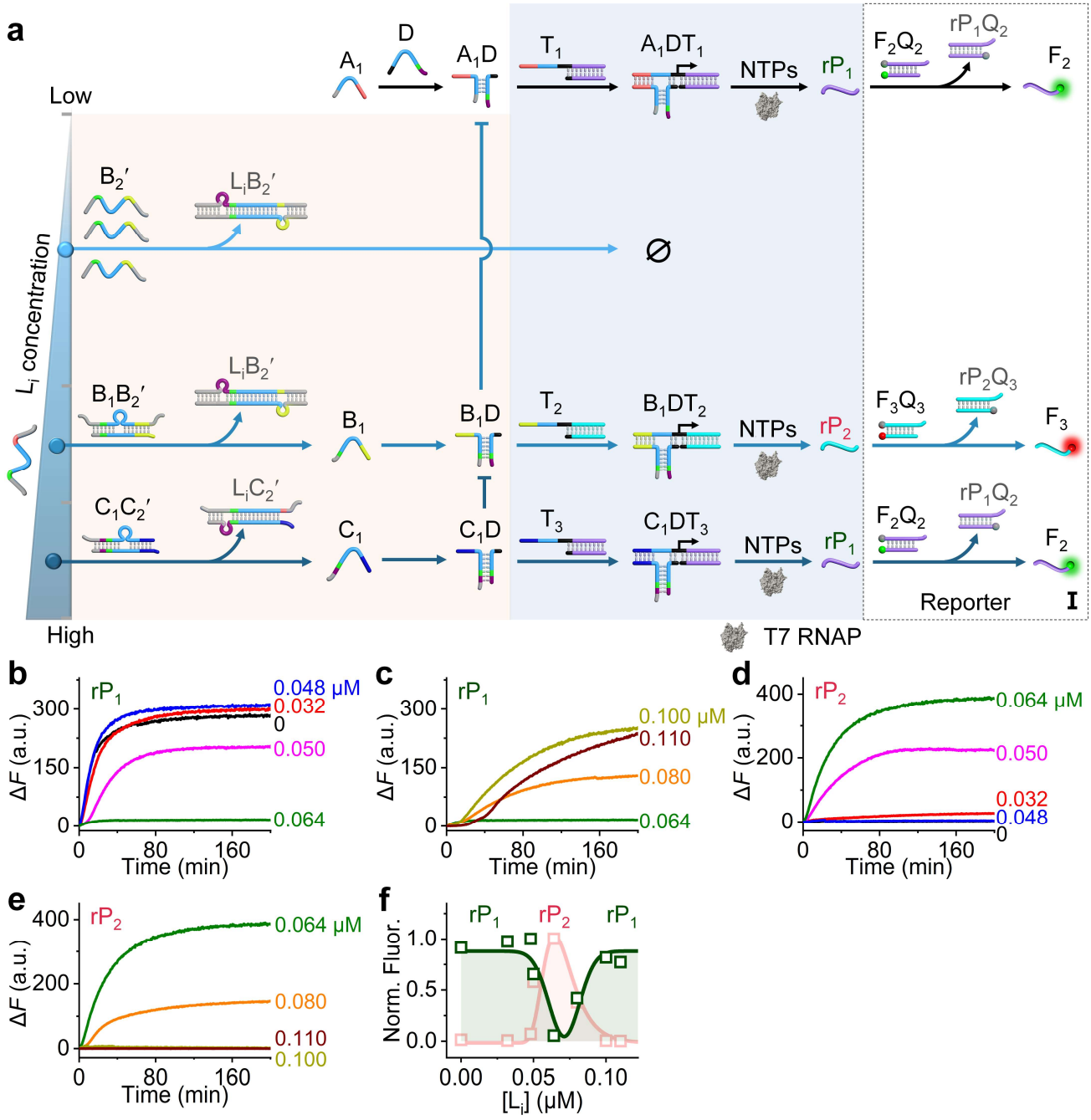
Supplementary Fig. 5 | TIFFN-III-dictated decoding of L_i concentration into discrete transcriptional states. a, Schematic illustrating the operation of the integrated architecture of TIFFN-III with its corresponding transcriptional actuation module, which translates increasing L_i concentration into discrete transcriptional states corresponding to rP_1, rP_2, and rP_3 outputs. Panel I—Schematic of RNA product detection via strand-displacement reactions using corresponding fluorescent reporters. **b**,**c**, Time-dependent FAM fluorescence changes reporting rP_1 transcription upon subjecting the system to different concentrations of L_i: 0, 0.010, and 0.016 μM (**b**); 0.016, 0.030, 0.044, 0.060, 0.080, and 0.110 μM (**c**). **d**,**e**, Time-dependent ROX fluorescence changes reporting rP_2 transcription upon subjecting the integrated architecture to different concentrations of input L_i: 0, 0.010, 0.016, 0.030, and 0.044 μM (**d**); 0.044, 0.060, 0.080, and 0.110 μM (**e**). **f**, Time-dependent Cy5 fluorescence changes reporting rP_3 transcription upon subjecting the integrated architecture to different concentrations of input L_i: 0, 0.010, 0.016, 0.030, 0.044, 0.060, 0.080, and 0.110 μM. **g**, Normalised fluorescence responses as a function of L_i concentration, derived from the results shown in **b**–**f**.



Supplementary Fig. 6 | TIFFN-I-mediated decoding of L_i concentration into discrete transcriptional states in the presence of additional 0.040 μM A_1'. a, Schematic showing the operation of the integrated architecture of TIFFN-I in the presence of additional 0.040 μM A_1' with its corresponding transcriptional actuation module, which converts increasing L_i concentration into discrete transcriptional states corresponding to none, rP_1, and rP_2 outputs. Panel I—Schematic of RNA output detection via strand-displacement reactions using corresponding fluorescent reporters. **b**,**c**, Time-dependent fluorescence changes of FAM reporting rP_1 transcription upon subjecting the integrated architecture to different concentrations of L_i: 0, 0.016, 0.032, 0.040, and 0.048 μM (**b**); 0.048, 0.060, 0.076, and 0.090 μM (**c**). **d**, Time-dependent fluorescence changes of ROX reporting rP_2 transcription upon subjecting the integrated architecture to different concentrations of L_i: 0, 0.016, 0.032, 0.040, 0.048, 0.060, 0.076, and 0.090 μM. **e**, Normalised fluorescence responses as a function of L_i concentration, derived from the results shown in **b**–**d**.

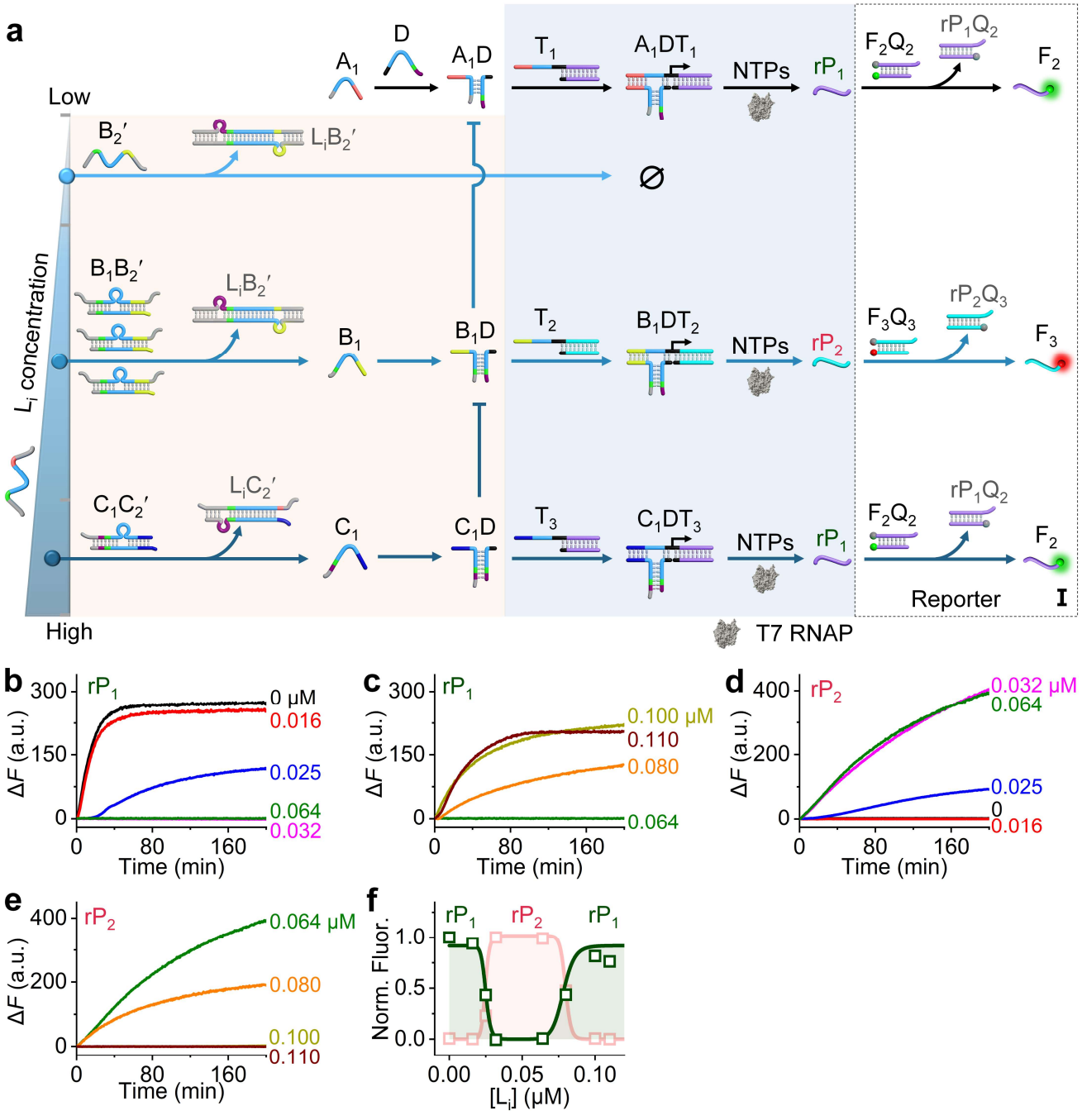


Supplementary Fig. 7 | TIFFN-I-governed decoding of L_i concentration into discrete transcriptional states in the presence of additional 0.040 μM A_1A_1'. a, Schematic illustrating the operation of the integrated architecture of TIFFN-I in the presence of additional 0.040 μM A_1A_1' with its corresponding transcriptional actuation module, which converts increasing L_i concentration into discrete transcriptional states corresponding to rP_1 and rP_2 outputs. Panel I—Schematic of RNA product detection via strand-displacement reactions using corresponding fluorescent reporters. **b**,**c**, Time-dependent changes in FAM fluorescence reporting rP_1 transcription upon subjecting the integrated architecture to different concentrations of L_i: 0, 0.010, 0.016, 0.032, and 0.048 μM (**b**); 0.048, 0.060, 0.076, and 0.090 μM (**c**). **d**, Time-dependent changes in ROX fluorescence reporting rP_2 transcription upon subjecting the integrated architecture to different concentrations of L_i: 0, 0.010, 0.016, 0.032, 0.048, 0.060, 0.076, and 0.090 μM. **e**, Normalised fluorescence responses as a function of L_i concentration, derived from the results shown in **b**–**d**.



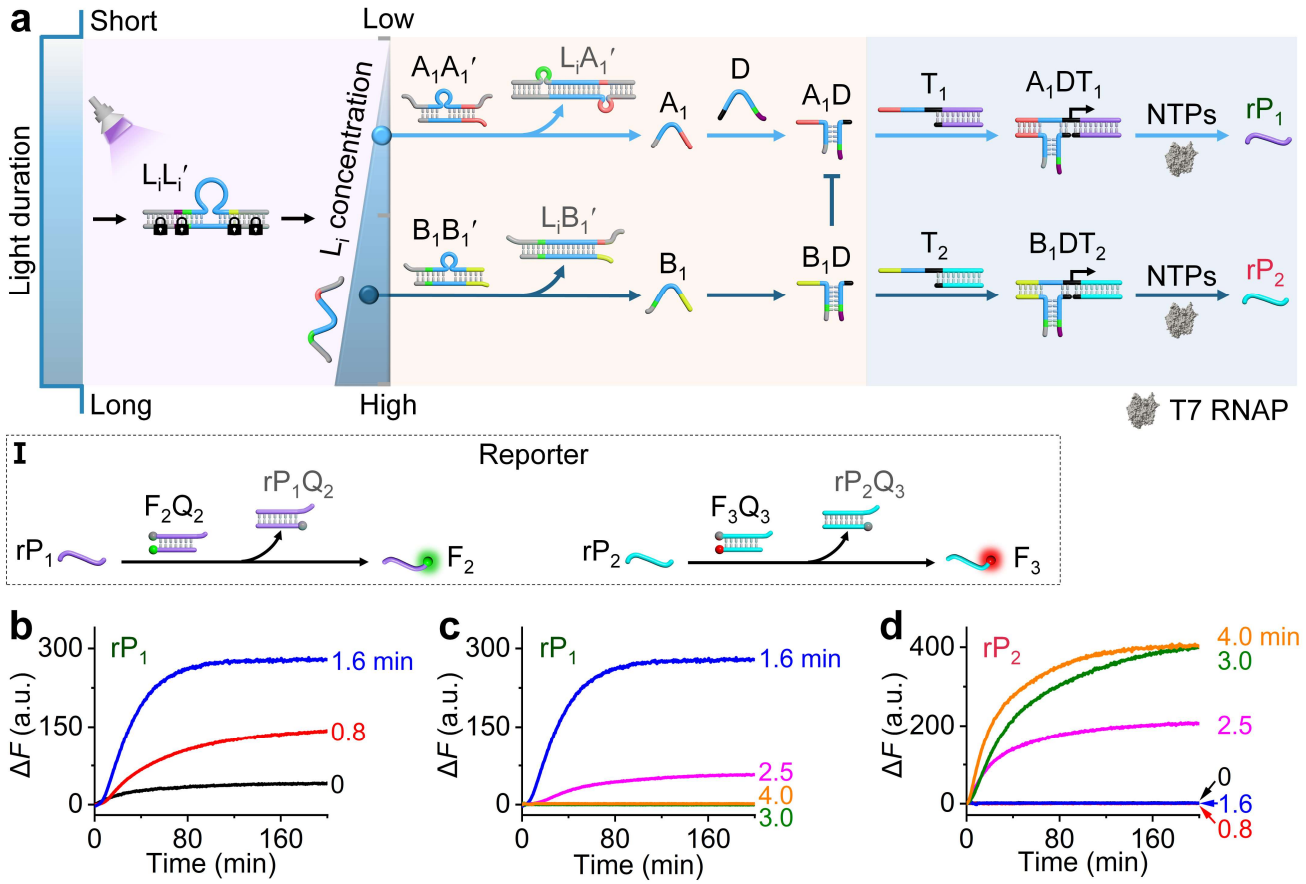
Supplementary Fig. 8 | TIFFN-II-mediated decoding of L_i concentration into discrete transcriptional states in the presence of additional 0.040 μM B_2'. a, Schematic illustrating the operation of the integrated architecture of TIFFN-II in the presence of additional 0.040 μM B_2' with its corresponding transcriptional actuation module, which converts increasing L_i concentration into discrete transcriptional states corresponding to rP_1, rP_2, and rP_1 outputs. Panel I—Schematic of RNA product detection via strand-displacement reactions using corresponding fluorescent reporters. **b**,**c**, Time-dependent FAM fluorescence changes reporting rP_1 transcription upon subjecting the integrated architecture to different concentrations of L_i: 0, 0.032, 0.048, 0.050, and 0.064 μM (**b**); 0.064, 0.080, 0.100, and 0.110 μM (**c**). **d**,**e**, Time-dependent ROX fluorescence changes reporting rP_2 transcription

upon subjecting the integrated architecture to different concentrations of L_i: 0, 0.032, 0.048, 0.050, and 0.064 μM (**d**); 0.064, 0.080, 0.100, and 0.110 μM (**e**). **f**, Normalised fluorescence responses as a function of L_i concentration, derived from the results shown in **b**–**e**.

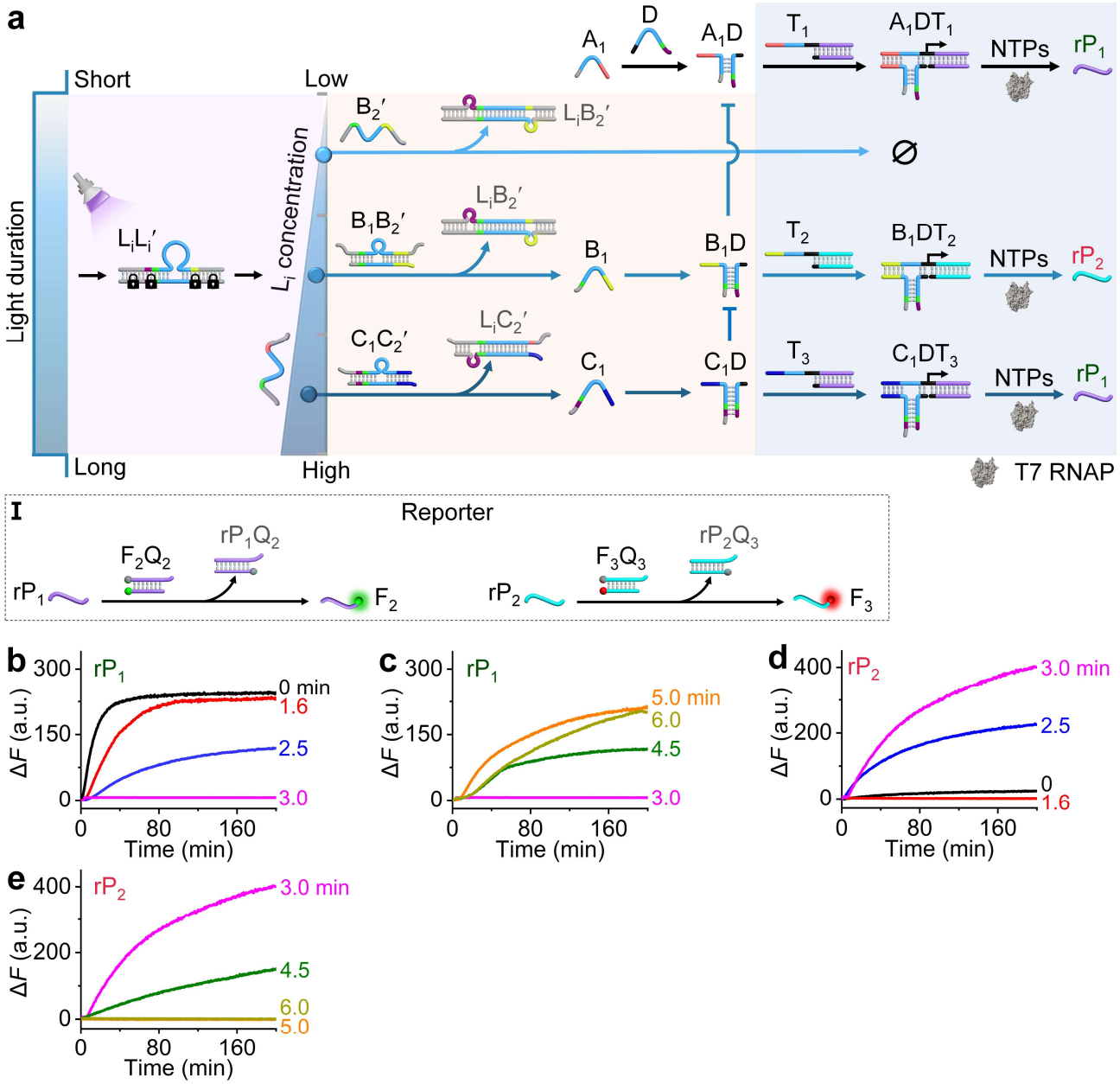


Supplementary Fig. 9 | TIFFN-II-governed decoding of L_i concentration into discrete transcriptional states in the presence of additional 0.040 μM B_1B_2'. a, Schematic showing the operation of the integrated architecture of TIFFN-II in the presence of additional 0.040 μM B_1B_2' with its corresponding transcriptional actuation module, which converts increasing L_i concentration into discrete transcriptional states corresponding to rP_1, rP_2, and rP_1 outputs. Panel I—Schematic of RNA

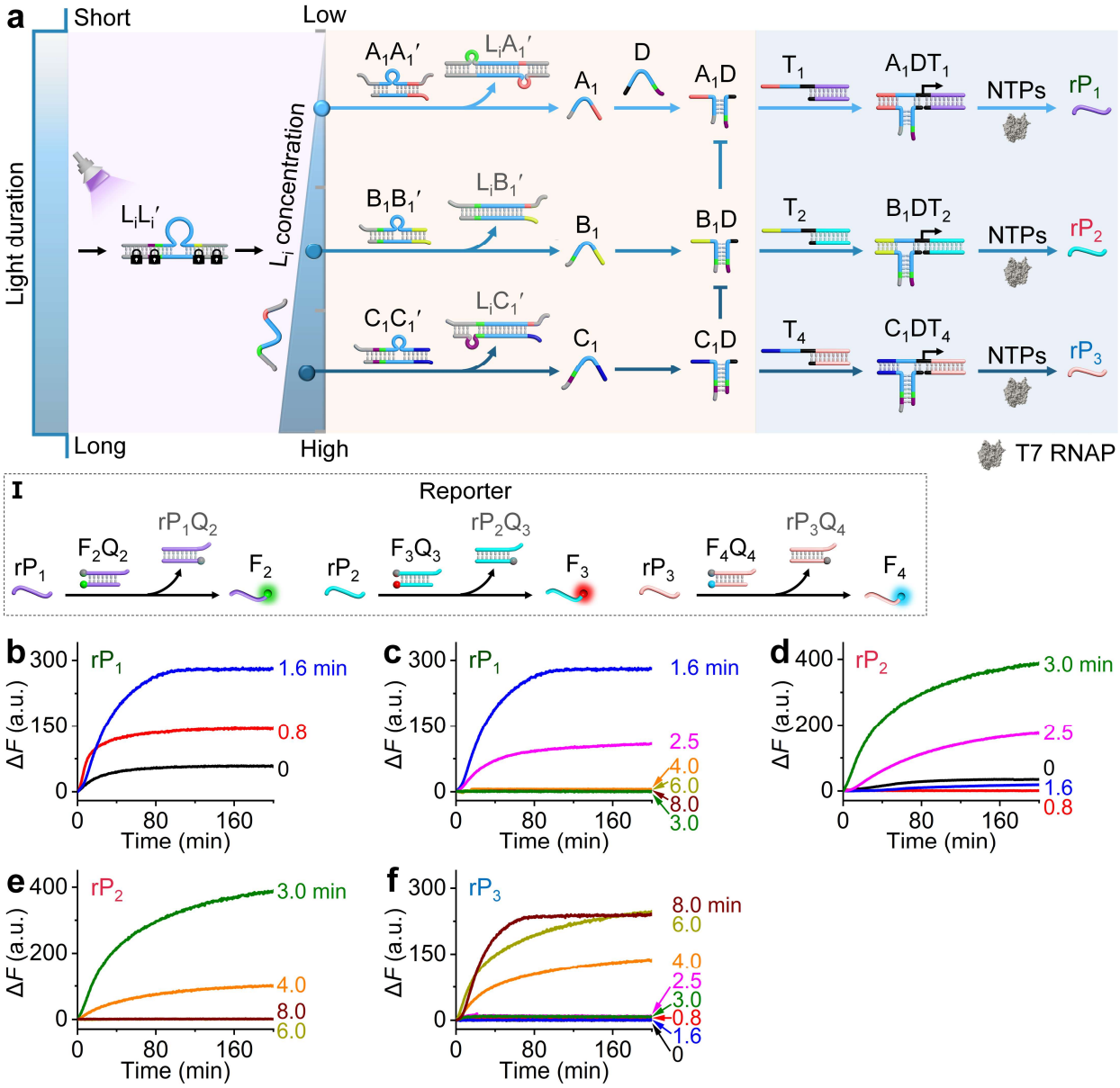
product detection via strand-displacement reactions using corresponding fluorescent reporters. **b**,**c**, Time-dependent changes in FAM fluorescence reporting rP_1 transcription upon subjecting the integrated architecture to different concentrations of L_i: 0, 0.016, 0.025, 0.032, and 0.064 μM (**b**); 0.064, 0.080, 0.100, and 0.110 μM (**c**). **d**,**e**, Time-dependent changes in ROX fluorescence reporting rP_2 transcription upon subjecting the integrated architecture to different concentrations of L_i: 0, 0.016, 0.025, 0.032, and 0.064 μM (**d**); 0.064, 0.080, 0.100, and 0.110 μM (**e**). **f**, Normalised fluorescence responses as a function of L_i concentration, derived from the results shown in **b**–**e**.



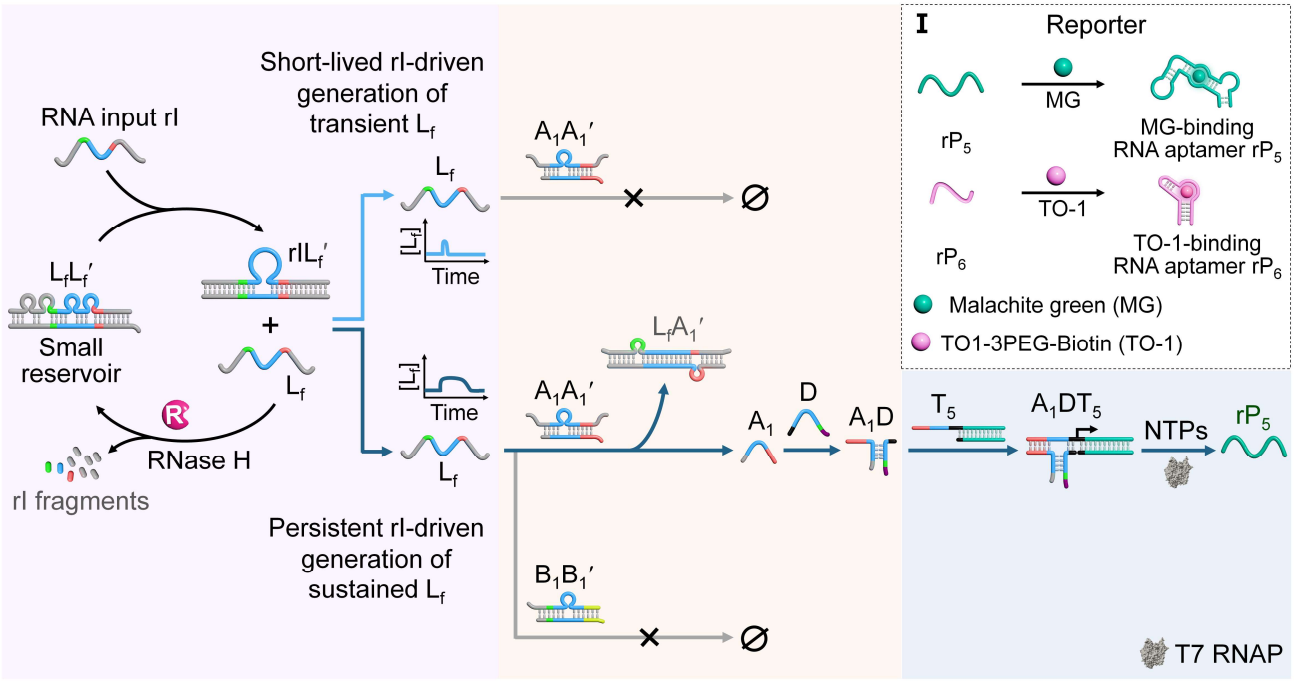
Supplementary Fig. 10 | piPDDS-I-dictated decoding of light duration into discrete transcriptional states. a, Schematic illustrating the operation of piPDDS-I consisting of a photochemical integration module, TIFFN-I module, and corresponding transcriptional actuation module, which translates light-duration information into discrete transcriptional states corresponding to rP_1 and rP_2 outputs. Panel I—Schematic of RNA product detection via strand-displacement reactions using corresponding fluorescent reporters. **b**,**c**, Time-dependent changes in FAM fluorescence reporting rP_1 transcription generated by the piPDDS-I architecture under different light durations: 0, 0.8, and 1.6 min (**b**); 1.6, 2.5, 3.0, and 4.0 min (**c**). **d**, Time-dependent changes in ROX fluorescence reporting rP_2 transcription generated by the piPDDS-I architecture under different light durations: 0, 0.8, 1.6, 2.5, 3.0, and 4.0 min.



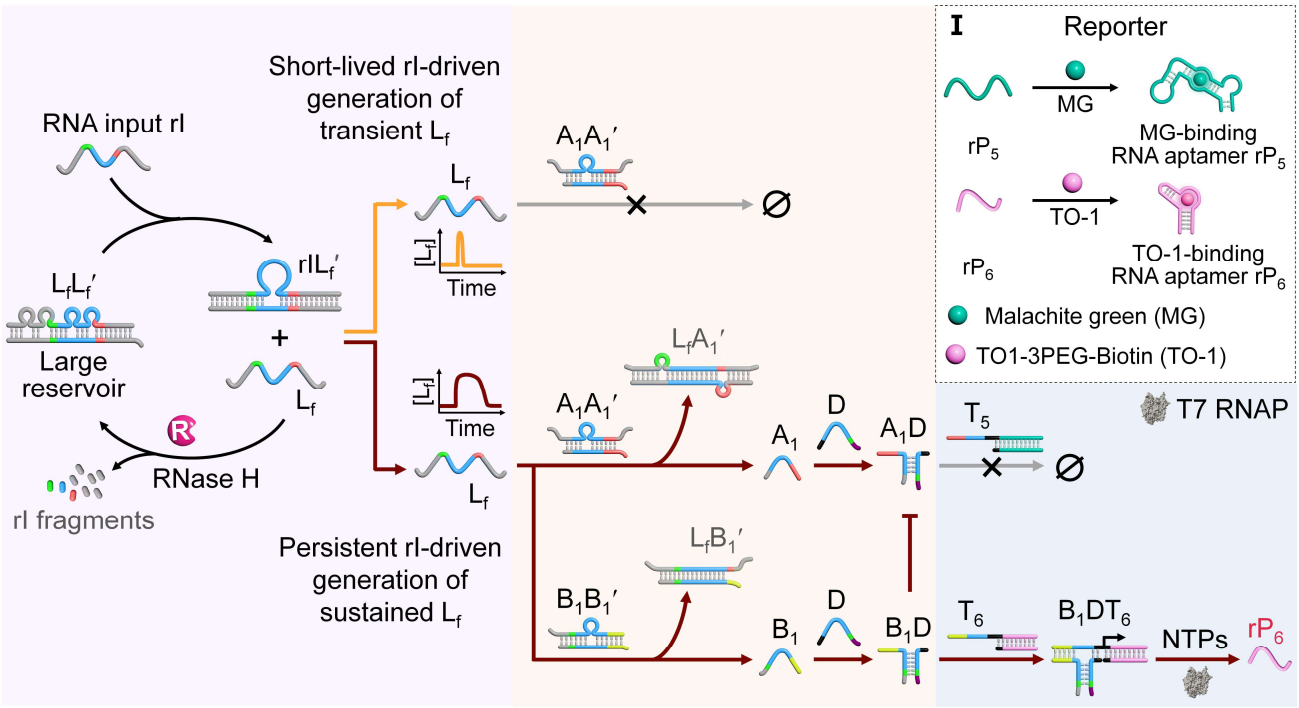
Supplementary Fig. 11 | piPDDS-II-governed decoding of light duration into discrete transcriptional states. a, Schematic showing the operation of piPDDS-II consisting of a photochemical integration module, TIFFN-II module, and corresponding transcriptional actuation module, which converts light-duration information into discrete transcriptional states corresponding to rP_1, rP_2, and rP_1 outputs. Panel I—Schematic of RNA product detection via strand-displacement reactions using corresponding fluorescent reporters. **b**,**c**, Time-dependent changes in FAM fluorescence reporting P_1 transcription generated by the piPDDS-II architecture under different light durations: 0, 1.6, 2.5, and 3.0 min (**b**); 3.0, 4.5, 5.0, and 6.0 min (**c**). **d**,**e**, Time-dependent changes in ROX fluorescence reporting rP_2 transcription generated by the piPDDS-II architecture under different light durations: 0, 1.6, 2.5, and 3.0 min (**d**); 3.0, 4.5, 5.0, and 6.0 min (**e**).



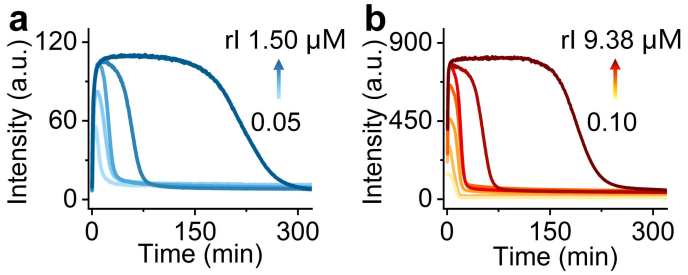
Supplementary Fig. 12 | piPDDS-III-mediated decoding of light duration into discrete transcriptional states. a, Schematic illustrating the operation of piPDDS-III consisting of a photochemical integration module, TIFFN-III module, and corresponding transcriptional actuation module, which translates light-duration information into discrete transcriptional states corresponding to rP_1, rP_2, and rP_3 outputs. Panel I—Schematic of RNA product detection via strand-displacement reactions using corresponding fluorescent reporters. **b**,**c**, Time-dependent changes in FAM fluorescence reporting rP_1 transcription generated by the piPDDS-III architecture under different light durations: 0, 0.8, and 1.6 min (**b**); 1.6, 2.5, 3.0, 4.0, 6.0, and 8.0 min (**c**). **d**,**e**, Time-dependent changes in ROX fluorescence reporting rP_2 transcription generated by the piPDDS-III architecture under different light durations: 0, 0.8, 1.6, 2.5, and 3.0 min (**d**); 3.0, 4.0, 6.0, and 8.0 min (**e**). **f**, Time-dependent changes in Cy5 fluorescence reporting rP_3 transcription generated by the piPDDS-III architecture under different light durations: 0, 0.8, 1.6, 2.5, 3.0, 4.0, 6.0, and 8.0 min.



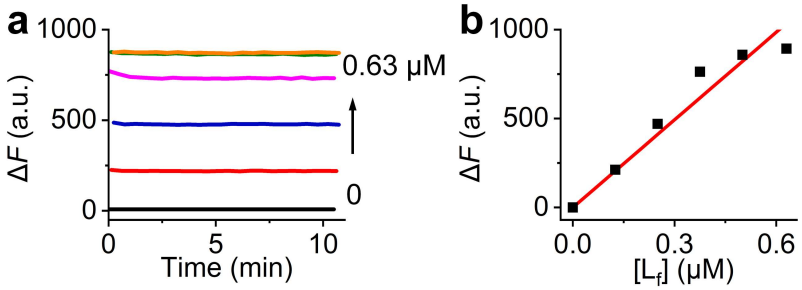
Supplementary Fig. 13 | Small reservoir-dictated dissipative RNA filtering transmits persistent RNA inputs into rP_5-output state. Schematic showing the operation of dfPDDS-I consisting of a dissipative RNA filtering layer with a small L_fL_f' reservoir, TIFFN-I-mediated decision-making, and corresponding transcriptional actuation. The system converts the RNA-input persistence into the transcriptional output, rP_5, by selectively transmitting persistent rI inputs while rejecting short-lived rI inputs. Panel I—Schematic of RNA aptamer-based fluorescence detection through ligand-binding-induced fluorescence activation.



Supplementary Fig. 14 | Large reservoir-dictated dissipative RNA filtering transmitting persistent RNA inputs into rP_6-output state. Schematic illustrating the operation of dfPDDS-I consisting of a dissipative RNA filtering layer with a large L_fL_f' reservoir, TIFFN-I-mediated decision-making, and corresponding transcriptional actuation. The system converts the RNA-input persistence into the transcriptional output, rP_6, by selectively transmitting persistent rI inputs while rejecting short-lived rI inputs. Panel I—Schematic of RNA aptamer-based fluorescence detection through ligand-binding-induced fluorescence activation.

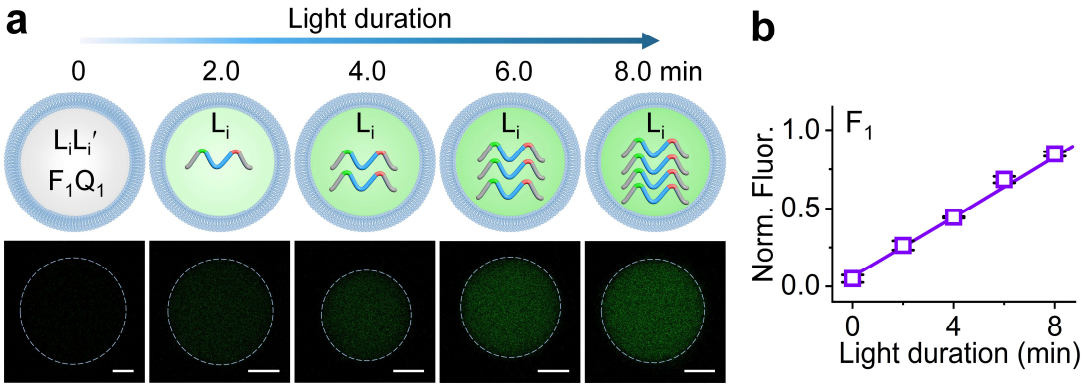


Supplementary Fig. 15 | Reservoir-programmed L_f pulse dynamics. a, Time-dependent changes in FAM fluorescence reporting L_f release upon subjecting the mixture of the small L_fL_f' reservoir (0.10 μM L_fL_f') and F_1Q_1 (0.63 μM) to RNA input rI with various concentrations. **b**, Time-dependent changes in FAM fluorescence reporting L_f release upon subjecting the mixture of the large L_fL_f' reservoir (0.63 μM L_fL_f') and F_1Q_1 (0.63 μM) to rI with various concentrations.

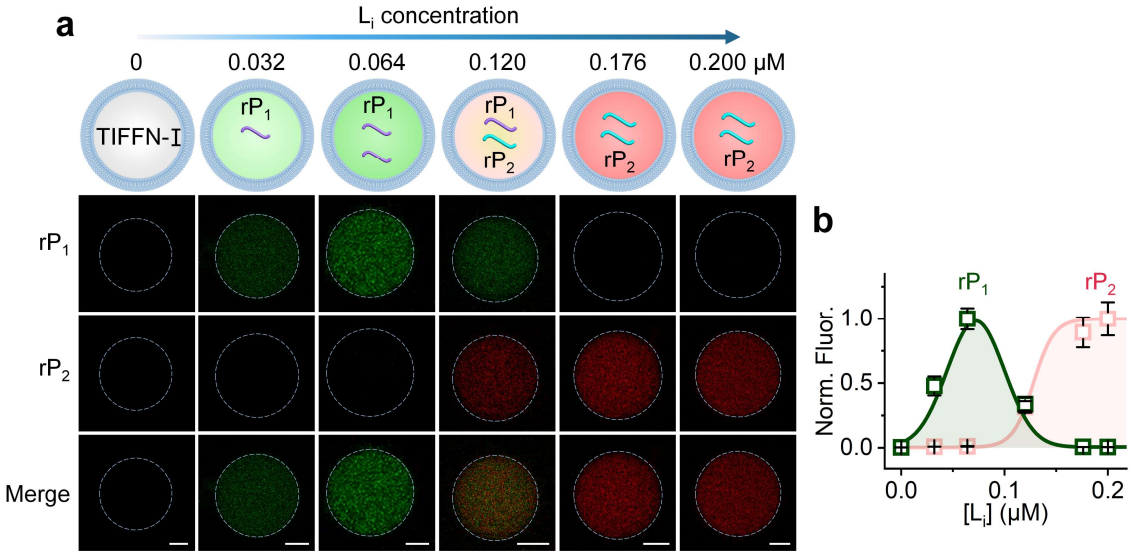


Supplementary Fig. 16 | Calibration curve of L_f. a, Time-dependent changes in FAM fluorescence reporting free L_f at various concentrations: 0, 0.13, 0.25, 0.38, 0.50, and 0.63 μM, in the presence of 0.63 μM F_1Q_1. **b**, Corresponding calibration curve of FAM fluorescence (λ_{em} = 516 nm) as a function of L_f concentration, derived from the results shown in **a**.

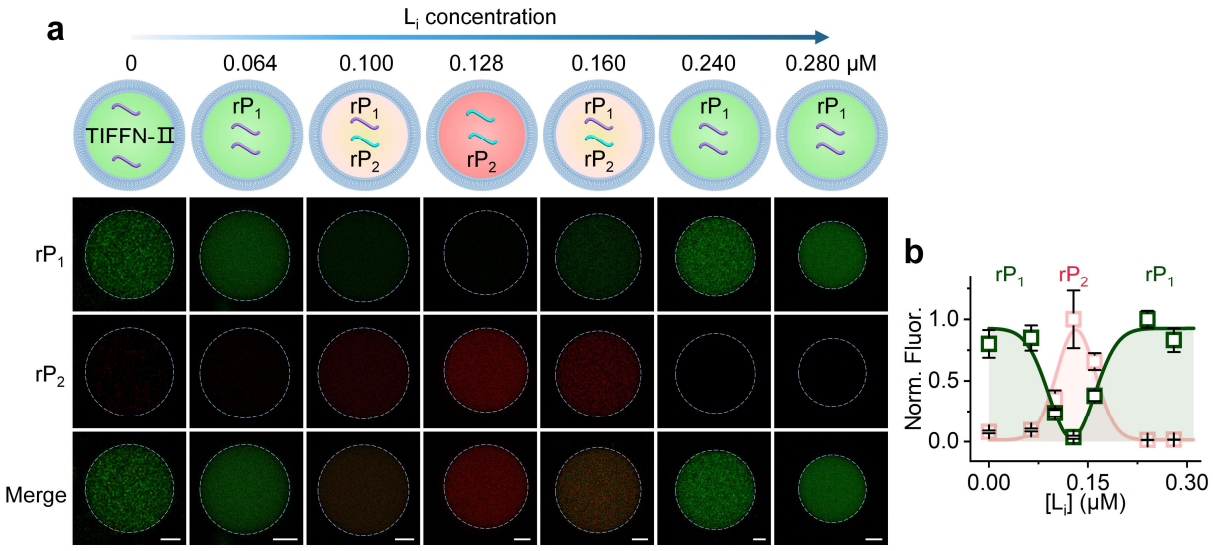
5. Characterisations of Duration-Decoding Programmed Distinct RNA-Output States in Synthetic Cells



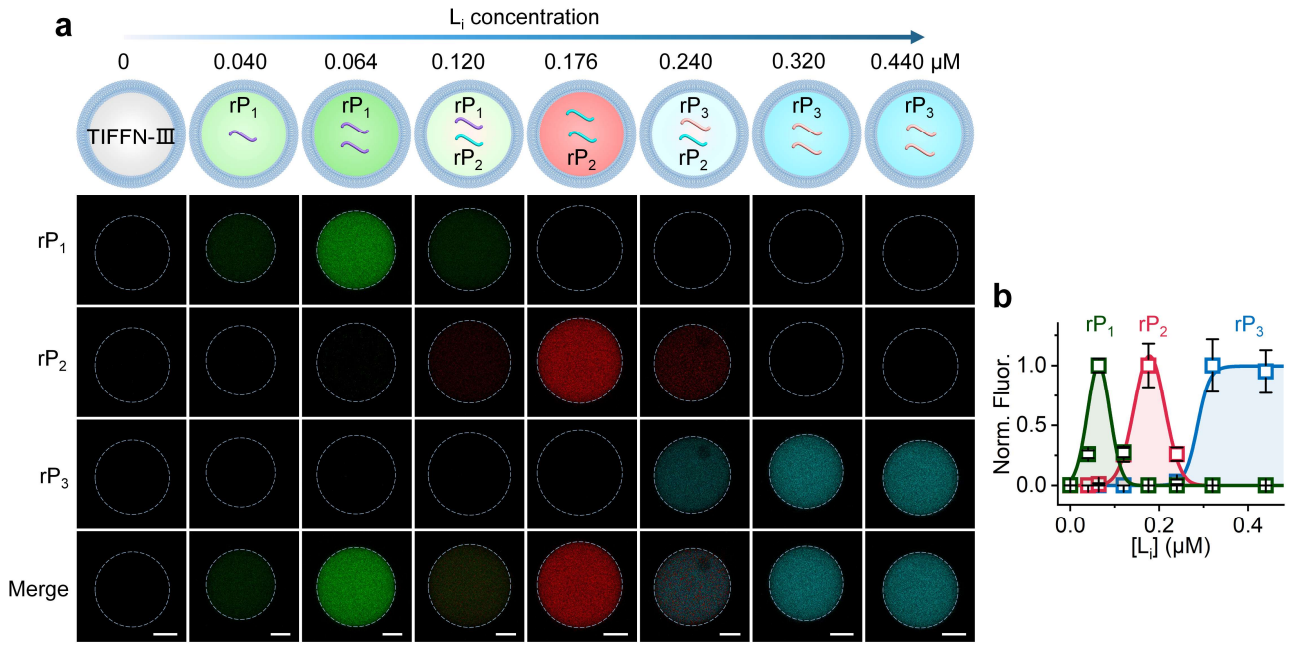
Supplementary Fig. 17 | Light-duration-dependent release of L_i in synthetic cells. a,**b**, Schematic and representative confocal images (**a**) and statistical analyses (**b**) depicting L_i release within the GUVs encapsulating L_iL_i' and F_1Q_1, under different light durations. Scale bars: 5 μm. Data in **b** are presented as mean ± s.d. of three independent experiments.



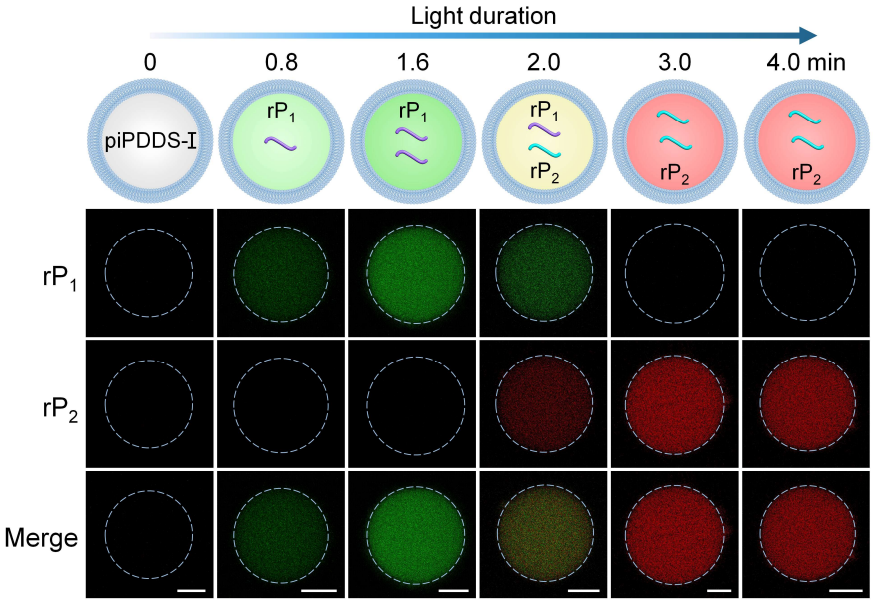
Supplementary Fig. 18 | TIFFN-I-mediated concentration-dependent differential transcription in synthetic cells. a,**b**, Schematic and representative confocal images (**a**) and statistical analyses (**b**) depicting the transcription levels of rP_1 and rP_2 within the GUVs encapsulating the integrated architecture of the TIFFN-I module with its corresponding transcriptional actuation module, and L_i at varying concentrations. Scale bars: 5 μm. Statistical data in **b** are presented as mean ± s.d. of three independent experiments.



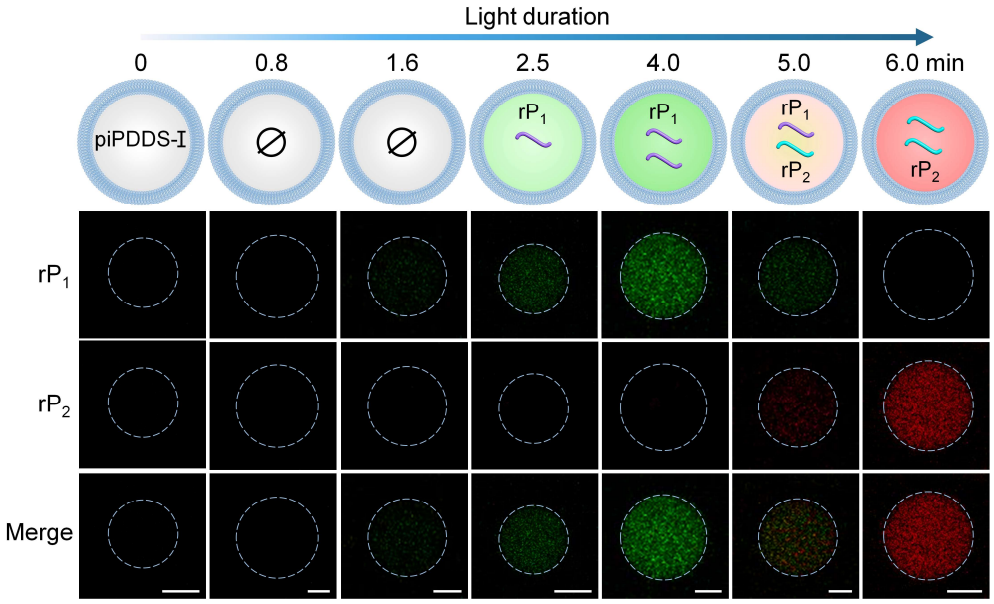
Supplementary Fig. 19 | TIFFN-II-dictated concentration-dependent differential transcription in synthetic cells. a,**b**, Schematic and representative confocal images (**a**) and statistical analyses (**b**) depicting the transcription levels of rP_1 and rP_2 within the GUVs encapsulating the integrated architecture of the TIFFN-II module with its corresponding transcriptional actuation module, and L_i at varying concentrations. Scale bars: 5 μm. Statistical data in **b** are presented as mean ± s.d. of three independent experiments.



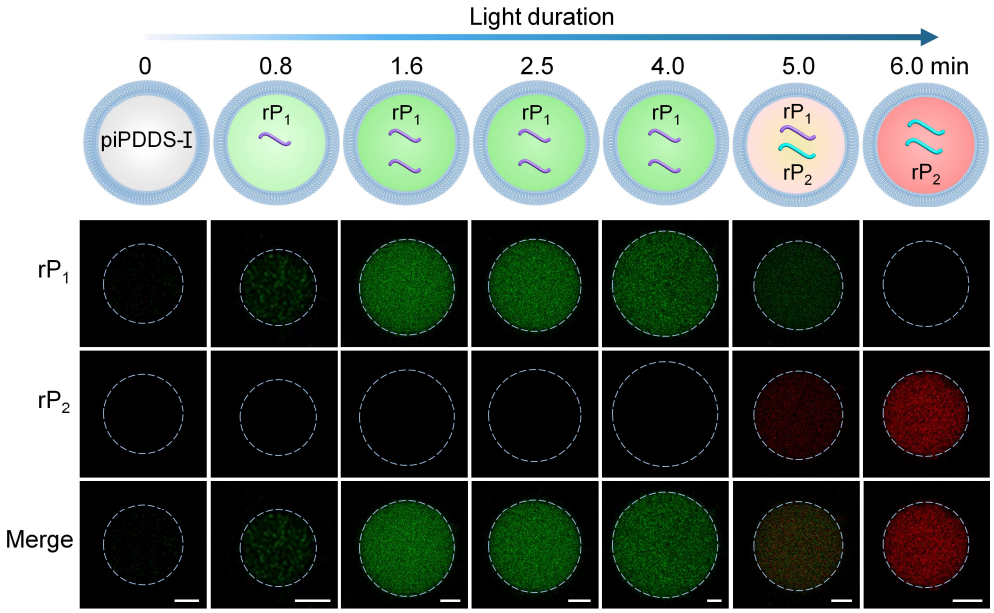
Supplementary Fig. 20 | TIFFN-III-dictated concentration-dependent differential transcription in synthetic cells. a,**b**, Schematic and representative confocal images (**a**) and statistical analyses (**b**) depicting the transcription levels of rP_1, rP_2, and rP_3 within the GUVs encapsulating the integrated architecture of the TIFFN-III module with its corresponding transcriptional actuation module, and L_i at varying concentrations. Scale bars: 5 μm. Statistical data in **b** are presented as mean ± s.d. of three independent experiments.



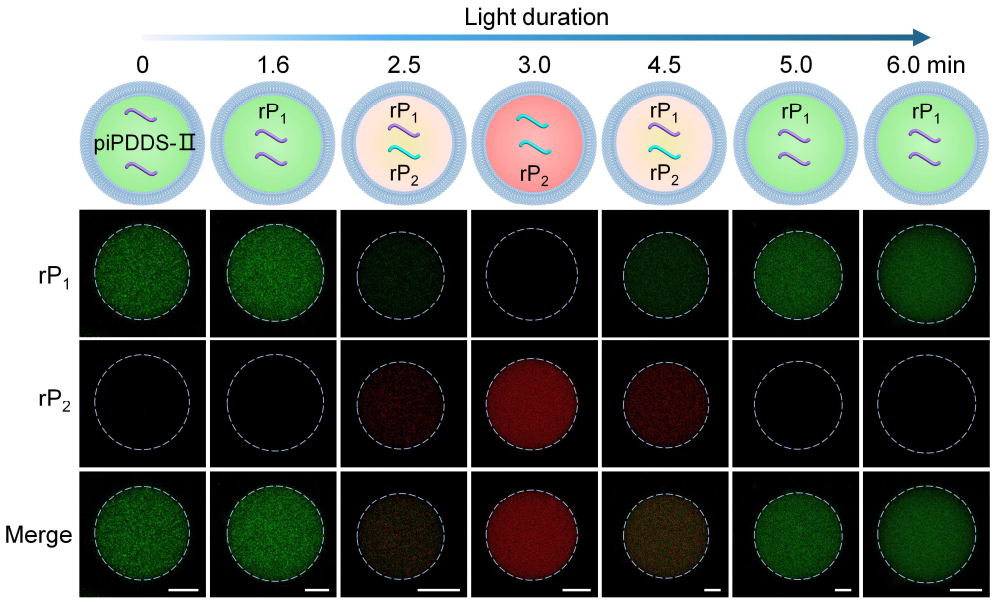
Supplementary Fig. 21 | piPDDS-I-governed duration-dependent differential transcription in synthetic cells. Schematic and representative confocal images depicting the transcription levels of rP_1 and rP_2 within the GUVs encapsulating piPDDS-I, under different light durations. Scale bars: 5 μm.



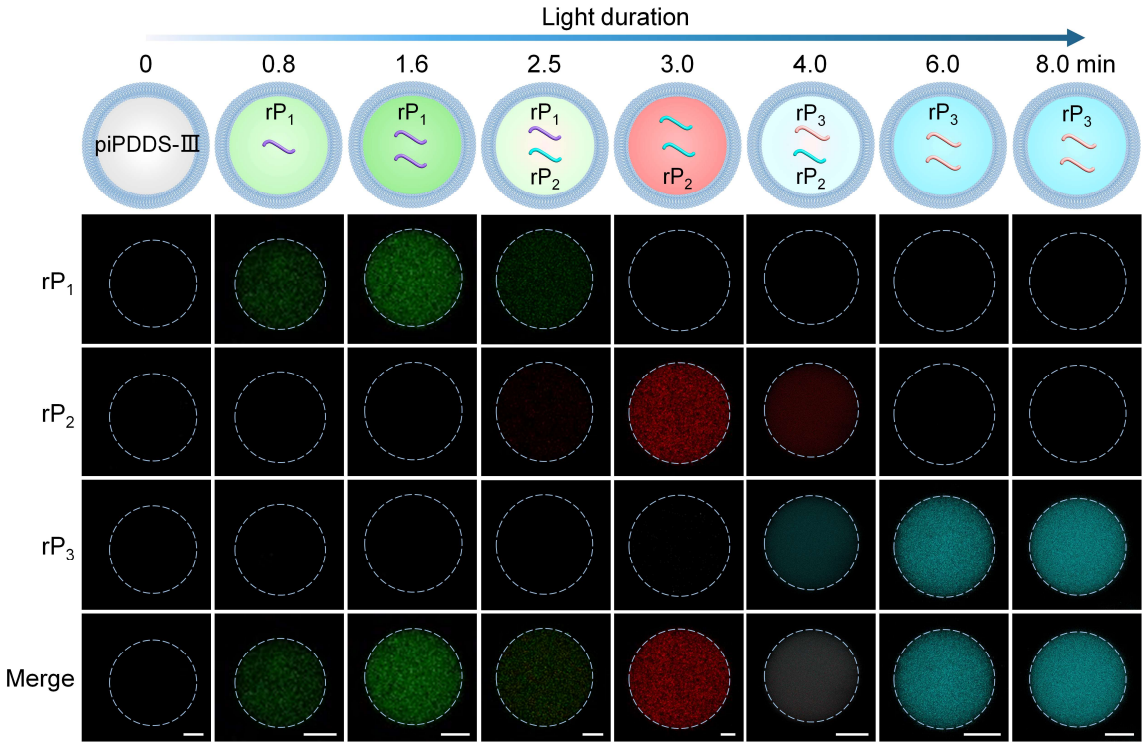
Supplementary Fig. 22 | piPDDS-I-governed duration-dependent differential transcription in synthetic cells in the presence of additional 0.16 μM A_1'. Schematic and representative confocal images depicting the transcription levels of rP_1 and rP_2 within the GUVs encapsulating piPDDS-I and additional 0.16 μM A_1', under different light durations. Scale bars: 5 μm.



Supplementary Fig. 23 | piPDDS-I-governed duration-dependent differential transcription in synthetic cells in the presence of additional 0.16 μM A_1A_1'. Schematic and representative confocal images depicting the transcription levels of rP_1 and rP_2 within the GUVs encapsulating piPDDS-I and additional 0.16 μM A_1A_1', under different light durations. Scale bars: 5 μm.

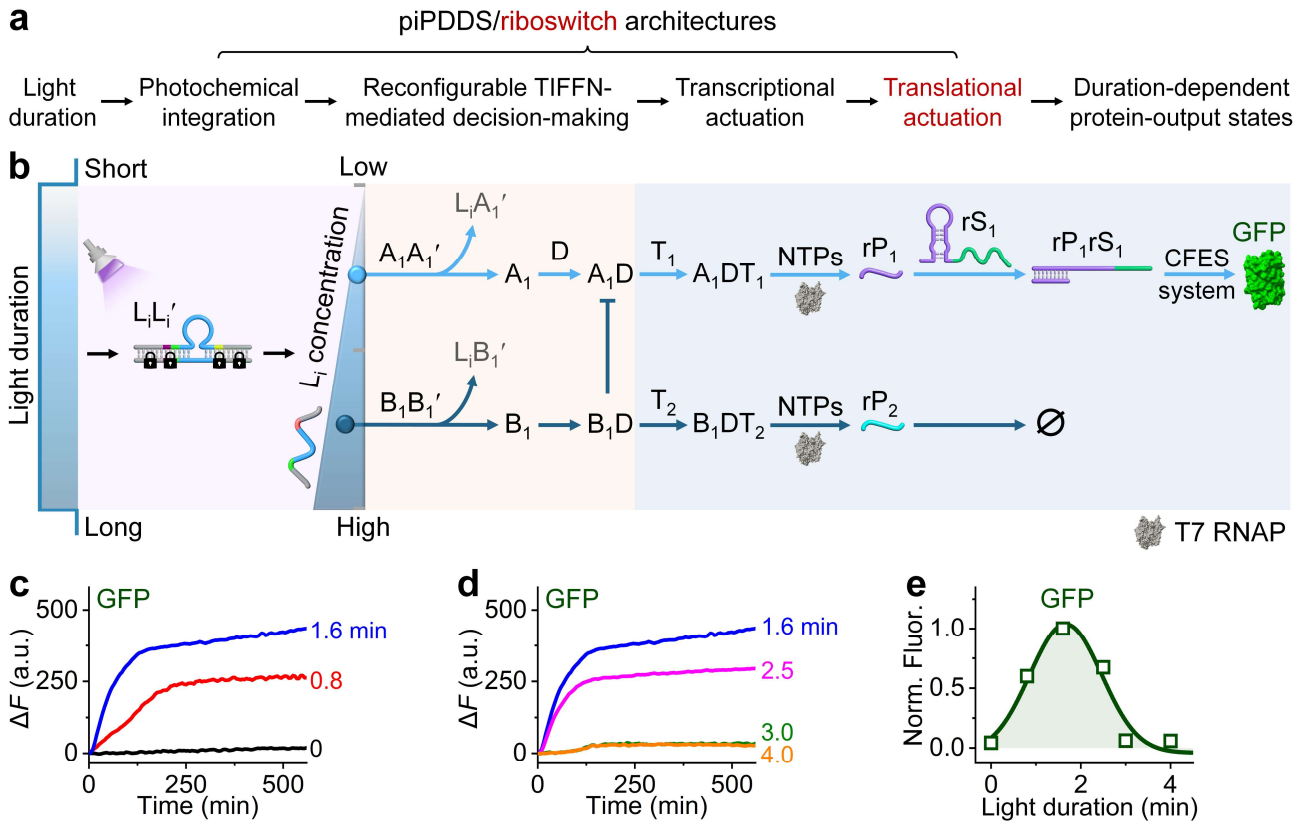


Supplementary Fig. 24 | piPDDS-II-governed duration-dependent differential transcription in synthetic cells. Schematic and representative confocal images depicting the transcription levels of rP_1 and rP_2 within the GUVs encapsulating piPDDS-II, under different light durations. Scale bars: 5 μm.

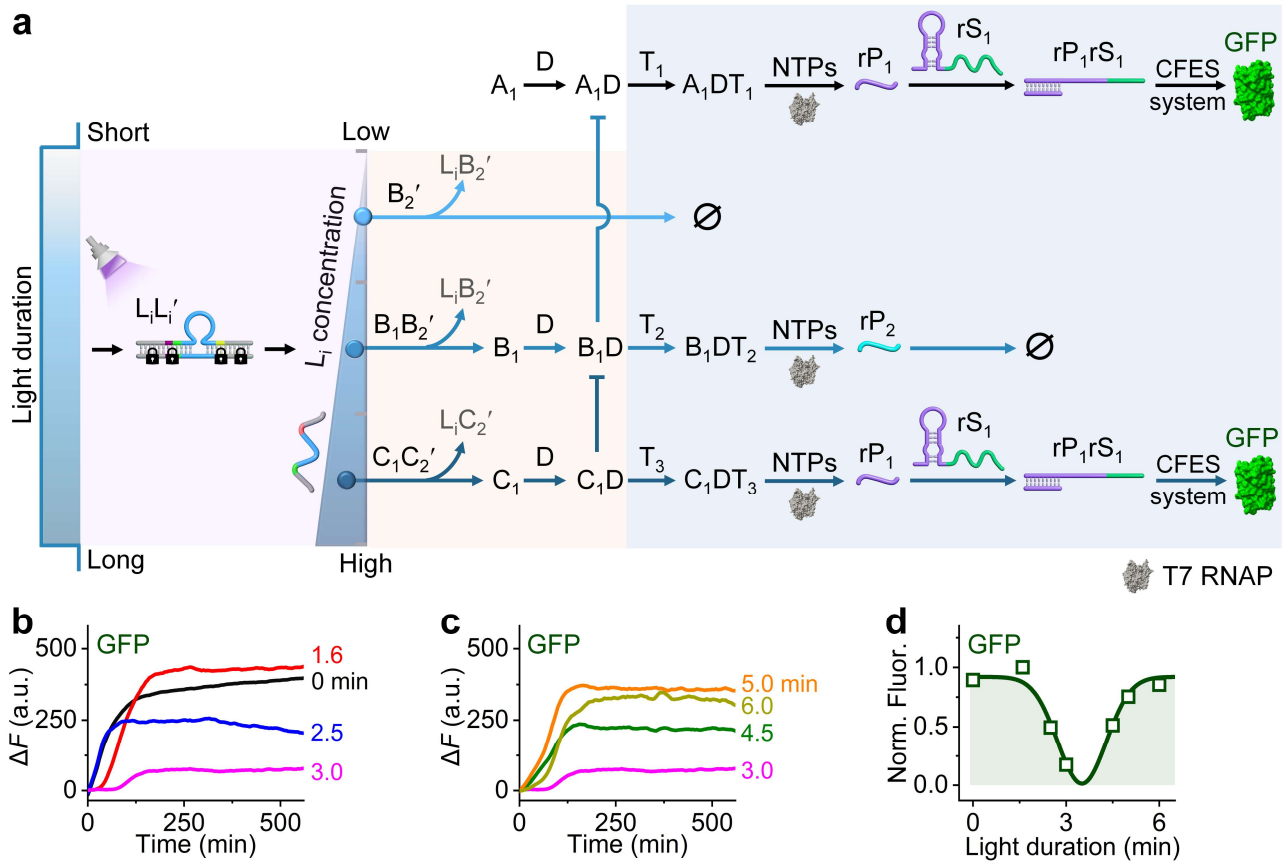


Supplementary Fig. 25 | piPDDS-III-governed duration-dependent differential transcription in synthetic cells. Schematic and representative confocal images depicting the transcription levels of rP_1, rP_2, and rP_3 within the GUVs encapsulating piPDDS-III, under different light durations. Scale bars: 5 μm.

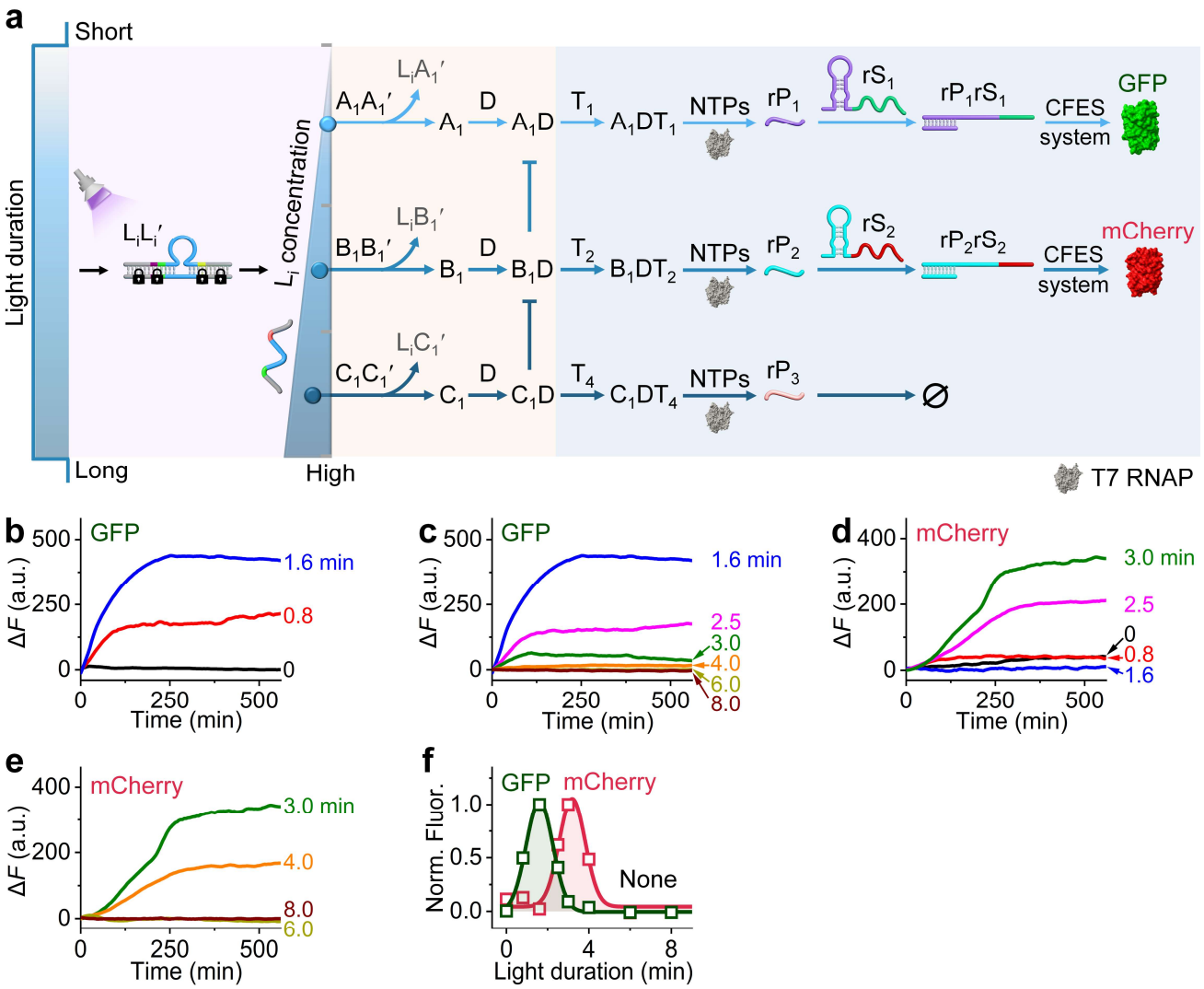
6. Characterisations of Duration Decoding Driven Differential Protein Synthesis in Synthetic Cells



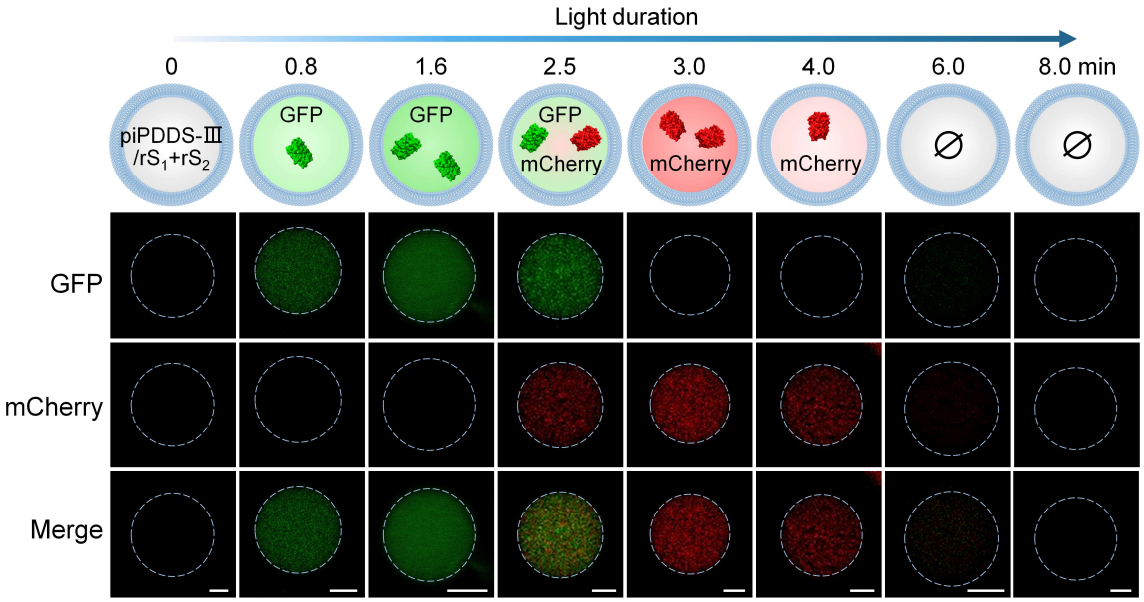
Supplementary Fig. 26 | Duration-windowed activation of GFP expression dictated by the integrated piPDDS-I/GFP-regulating riboswitch architecture. a, Flowchart showing the operation of the integrated piPDDS/riboswitch architectures to convert light duration into distinct protein outputs through sequential photochemical integration, reconfigurable TIFFN-mediated decision-making and downstream transcriptional and translational actuation. **b**, Schematic illustrating the operation of the integrated piPDDS-I/GFP-regulating riboswitch architecture, which translates increasing light durations into windowed activation of GFP expression. **c**,**d**, Time-dependent fluorescence changes of expressed GFP generated by the integrated architecture under different light durations: 0, 0.8, and 1.6 min (**c**); 1.6, 2.5, 3.0, and 4.0 min (**d**). **e**, Normalised fluorescence responses as a function of light duration, derived from the results shown in **c** and **d**.



Supplementary Fig. 27 | Duration-windowed repression of GFP expression governed by the integrated piPDDS-II/GFP-regulating riboswitch architecture. a, Schematic illustrating the operation of the integrated piPDDS-II/GFP-regulating riboswitch architecture consisting of a photochemical integration layer, a TIFFN-II layer, and a transcriptional and translational actuation layer, which translates increasing light durations into windowed repression of GFP expression. **b**,**c**, Time-dependent fluorescence changes of expressed GFP generated by the integrated architecture under different light durations: 0, 1.6, 2.5, and 3.0 min (**b**); 3.0, 4.5, 5.0, and 6.0 min (**c**). **d**, Normalised fluorescence responses as a function of light duration, derived from the results shown in **b** and **c**.

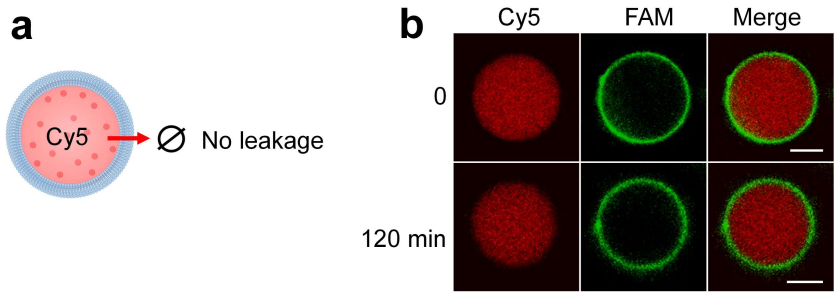


Supplementary Fig. 28 | Duration-decoding into distinct protein outputs mediated by the integrated piPDDS-III/GFP- and mCherry-regulating riboswitch architecture. a, Schematic illustrating the operation of the integrated piPDDS-III/GFP- and mCherry-regulating riboswitch architecture consisting of a photochemical integration layer, a TIFFN-III layer, and a transcriptional and translational actuation layer, which converts increasing light duration into discrete translational states corresponding to GFP, mCherry, and none outputs. **b**,**c**, Time-dependent fluorescence changes of expressed GFP generated by the integrated architecture under different light durations: 0, 0.8, and 1.6 min (**b**); 1.6, 2.5, 3.0, 4.0, 6.0, and 8.0 min (**c**). **d**,**e**, Time-dependent fluorescence changes of expressed mCherry generated by the integrated architecture under different light durations: 0, 0.8, 1.6, 2.5, and 3.0 min (**d**); 3.0, 4.0, 6.0, and 8.0 min (**e**). **f**, Normalised fluorescence responses as a function of light duration, derived from the results shown in **b**–**e**.

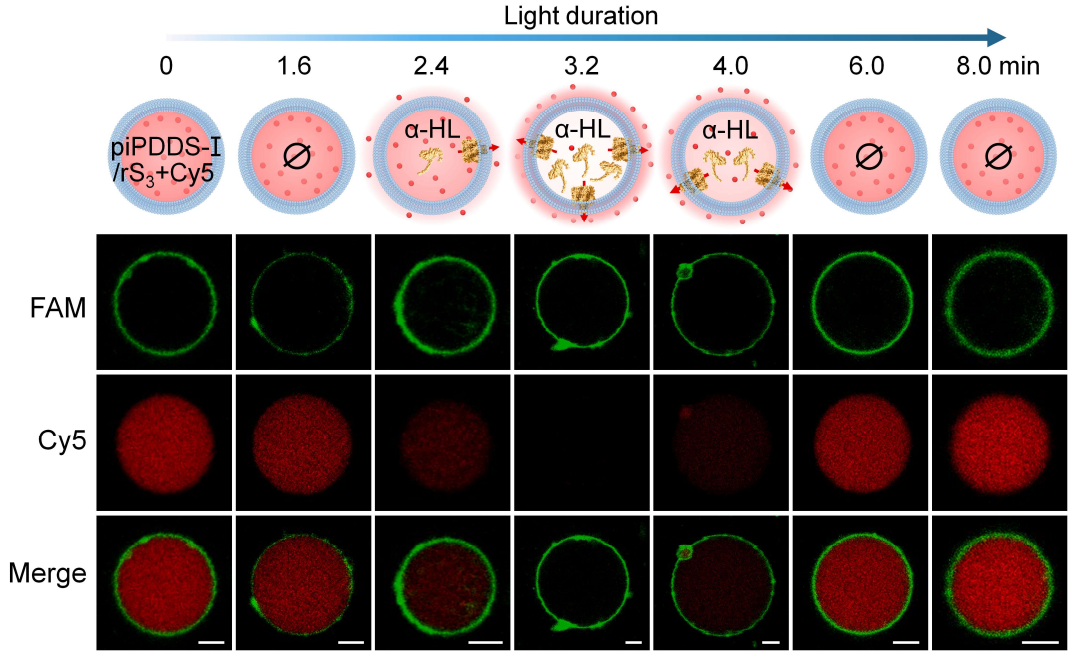


Supplementary Fig. 29 | piPDDS-III-governed duration-dependent differential protein synthesis in synthetic cells. Schematic and representative confocal images depicting the translation levels of GFP and mCherry within the GUVs encapsulating the integrated piPDDS-III/rS_1+rS_2 architecture, under different light durations. Scale bars: 5 μm. rS_1 and rS_2 denote the GFP-regulating riboswitch and the mCherry-regulating riboswitch, respectively.

7. Characterisations of Duration-Windowed Lipid Membrane Permeabilisation



Supplementary Fig. 30 | Baseline permeability of GUV lipid membranes in the absence of α-HL. **a**, Schematic showing passive Cy5 leakage from GUVs encapsulating Cy5 as a model cargo. **b**, Representative confocal images of GUVs containing Cy5 cargo and FAM-labelled lipid bilayers after incubation at 37 °C for 0 and 120 min.



Supplementary Fig. 31 | piPDDS-I-governed duration-windowed membrane permeabilisation in synthetic cells. Schematic and representative confocal images depicting FAM-labelled GUV membranes and Cy5 cargo release from GUVs encapsulating the integrated piPDDS-I/rS_3 architecture and cargo Cy5, under different UV irradiation durations. Scale bars: 5 μm. rS_3 denotes the α-HL-regulating riboswitch.